Numerical and experimental analysis of pressure fluctuation in axial flow turbine

Cite as: AIP Advances **12**, 025122 (2022); https://doi.org/10.1063/5.0071123
Submitted: 12 September 2021 • Accepted: 28 January 2022 • Published Online: 16 February 2022

Yanjun Li, Israel Enema Ohiemi, Punit Singh, et al.

Numerical and experimental analysis of pressure fluctuation in axial flow turbine

Cite as: AIP Advances 12, 025122 (2022); doi: 10.1063/5.0071123
Submitted: 12 September 2021 • Accepted: 28 January 2022 •
Published Online: 16 February 2022

Yanjun Li,[1] Israel Enema Ohiemi,[1,2,a)] Punit Singh,[3] and Yang Sunsheng[1]

AFFILIATIONS

[1] National Research Centre of Pumps, Jiangsu University, Zhenjiang 212013, China
[2] Department of Mechanical Engineering, University of Nigeria, Nsukka 410001, Nigeria
[3] Centre for Sustainable Technologies, Indian Institute of Science, CV Raman Road, Bangalore 560012, India

[a)] **Author to whom correspondence should be addressed:** israel.ohiemi@unn.edu.ng

ABSTRACT

The operational stability of axial flow turbines (AFT) directly affects its safety and performance. Hence, dynamic analysis of its internal flow characteristics is essential, since its unsteady pressure characteristics are complicated. A reliable measurement approach becomes essential in order to analyze and understand the pressure fluctuation within the turbine. Dynamic pressure pulsation measurements were conducted by installing pressure sensors on the flow domain of the AFT under different operating conditions. Based on computational and experimental measurements, different unsteadiness in the flow structures resulted in various excitation signals. The excited frequencies of the stationary parts occurred at 72.50 Hz ($3 \times f_n$), 145.00 Hz ($6 \times f_n$), and 217.50 Hz ($9 \times f_n$), while for the impeller, excited frequencies of 217.50 Hz ($9 \times f_n$), 435.00 Hz ($18 \times f_n$), and 652.50 Hz ($27 \times f_n$) were recorded. The rotor–stator interaction with fluid flow from the guide vane to the impeller is culpable for strong pressure pulsations. The experimental measurement shows a comprehensive agreement with numerical results. This paper focused on the analysis of pressure fluctuation in AFT combining experimental and computational methods. Moreover, an exhaustive understanding of flow characteristics of the AFT is necessary for its optimization and operational reliability.

I. INTRODUCTION

An axial flow turbine (AFT) is a propeller or Kaplan turbine that can run at a low head and under large flow rate. Due to its appropriateness for low head and high flow rate conditions, AFT offers a wide range of applications. The turbine's flow characteristics are complicated, with turbulent and vortex flow, rendering it vulnerable to unsteady pressure. Energy demand fluctuations have forced a number of power plants to operate in an off-design mode with changing loads.[1] The pressure fluctuation behavior of a turbomachinery is directly affected by the varied unsteadiness of the flow structure inside it, resulting in a range of excitation signals.[2] The turbine's transient operation causes pressure pulsations, which lead to uneven load distribution on the blades of the impeller.[3] As a result, the irregular load distribution has an impact on the turbine's life cycle, increase pressure losses, and reduces the turbine's efficiency.[3,4] During transient operation at different operating conditions, experimental investigation by previous researchers established the occurrence of large amplitudes in turbomachines.[3–6] Regardless of the axial distance between the rotor and guiding vanes (GVs), pressure pulsations within the flow channels of AFT are significantly influenced by the guide vane.[7,8]

The excitation of a particular pattern of impeller vibration is basically caused by combination of the impeller cascade with a static guide vane.[9] The reactive exchange of periodic forces varying with time, fundamental frequency, and a level of harmonics with respect to the number of blades in each cascade and shaft rotational speed represents the interaction of these two cascades.[9,10]

Using several turbulence models, Javadi and Nilsson[11] numerically provided a thorough rotor–stator interaction (RSI) study on an AFT. Kim *et al.*[12] investigated flow characteristics on the blade tip clearance of an AFT under various operating flow conditions using transient flow modeling and fast Fourier transform (FFT). Using the large eddy simulation, Sang *et al.*[13] experimentally confirmed the numerical study of the rotor–stator interaction (RSI) on radial forces of a two-stage axial flow blood pump. Zhang *et al.*[14,15] used

numerical analysis to analyze the failure of an AFT and compared the natural frequencies of the damaged and uncracked impellers. The impact of a floor-attached vortex on pressure variations in an axial flow pump was investigated by Song and Liu.[16,17] Shi *et al.*[18] examined the difference in pressure fluctuations in an axial flow and tubular pump using both experimental and computational methods. They found that the tubular pump's intake area had more pressure pulsations than the axial flow pumps.

A. Problem statement

The background literature indicates that the turbine's operational stability is influenced by unsteady flow pulsation, which has an impact on its operational safety. The inlet pipe of low head axial flow turbine is influenced by diverse design situation since designers need to factor in where to position the alternator. The above factor opens up two case scenarios that are essential for system design and plant load in specific cases. The first case scenario is the choice of right angled (90° bend) inlet and second the inline (straight) entry.

Furthermore, the effect of geometrical variations in the guiding vanes on harmonics of the pulsations within the turbine requires critical investigation in order to disclose the turbine's 3D unsteady flow characteristics.

A complete analysis of the turbine's unsteady flow pressure variations using computational and experimental approaches is required. In view of the above, the Shear Stress Transport (SST) k-turbulence model in conjunction with statistical techniques would be used to examine pressure fluctuations under various geometric and flow conditions. The findings may be used as reference for AFT design and as an operational guide to assure the turbine's safe functioning.

B. Research objectives

(1) To disclose the 3D unsteady flow characteristics of the turbine with the right-angled inlet pipe. This consists of a complete analysis of the turbine's unsteady flow pressure variations using computational and experimental approaches. The Shear Stress Transport (SST) k-turbulence model, in conjunction with statistical techniques, would be employed to examine the pressure fluctuations under various flow conditions.
(2) To numerically study the effect of change in the number of guide vanes of the turbine on pressure pulsations and examine its resultant effect on harmonics patterns in its frequency domain history.
(3) To numerically investigate the effect of straight inlet pipe on pressure pulsations and compare it to the pulsation patterns recorded by right-angled (90° bend) inlet pipe.
(4) To compare the variations in the distribution of velocity fluctuation intensities in the guide vane of the turbine due right-angled and straight inlet pipes.

II. THEORETICAL CONCEPT OF UNSTEADY FLOW FIELD AND EIGENMODE

The flow field in turbomachinery is time periodic and is mostly seen as a superposition of transient perturbation on a steady non-uniform mean flow.[19] Hence, a linear frequency-domain analysis, which enables individual blade-to-blade passage investigation, is employed.

The dominant unsteadiness in the flow is time periodic and small. As a result, the unsteadiness in the flow is first decomposed into a non-uniform steady but mean flow with time-periodic disturbances defined by distinctive frequency, which manifest as the blade vibration frequency or a multiple of the blade passing frequency (BPF) in forced response.[20–22] It is thought that this has a low amplitude and a characteristic frequency that is different from the frequencies of the aeroelastic phenomena under investigation. In order to eliminate the dependency of time, the equations of the flow were linearized time series and transformed into frequency domain. It is important to compute the steady flow on which the linearization will be conducted first and then to execute a separate linear calculation for each frequency of interest.

It is possible to model the unsteadiness within a single blade cascade on extended regions upstream and downstream. However, numerical solutions must be determined on an abridged finite domain in practice. To correctly simulate the unbounded character of the distant field, it is critical that the unsteadiness radiating out from the blade row is not artificially mirrored at both extremes of the finite domain.

A. Eigenmode equations

This section covers a brief theoretical concept of the eigenmode analysis for turbomachinery applications. For more detail concept of the eigenmode, please refer to Refs. 20–22. The 3D Euler equations[21] in both conservative and cylindrical coordinates are presented as

$$\frac{\partial Q_c}{\partial t} + \frac{1}{r}\frac{\partial}{\partial r}(rF_r) + \frac{1}{r}\frac{\partial F_\theta}{\partial \theta} + \frac{\partial F_x}{\partial x} = G, \tag{1}$$

where $Q_c, F_r, F_\theta, F_x, G$ represent the conservative variables, radial flux, circumferential flux axial flux, and source term (Coriolis and centrifugal forces).

Equation (1) is linearized about the mean flow, axially and circumferentially to obtain the following equation:

$$M\frac{\partial y}{\partial x} + \frac{1}{r}\frac{\partial}{\partial r}(rA_rQ_p) + \frac{1}{r}A_\theta\frac{\partial Q_p}{\partial \theta} + A_x\frac{\partial Q_p}{\partial x} = SQ_p. \tag{2}$$

The perturbation vector Q_p is dependent on density, velocity, and pressure, but $M = \frac{\partial Q_c}{\partial Q_p}$. Furthermore, M, A_r, A_x, A_θ, and S are matrices, which are all functions of the radius r.

Therefore, the eigenmodes are presented as

$$Q_p = \exp(iwt + im\theta + ikx)Q_p(r). \tag{3}$$

ω represents the frequency of either vibration frequency or an incoming wave. Substituting Eq. (3) into Eq. (2) gives

$$iwMQ_p + \frac{1}{r}\frac{\partial}{\partial r}(rA_rQ_p) + \frac{1}{r}imA_\theta Q_p + ikA_xQ_p = SQ_p. \tag{4}$$

B. Normal mode

The normal vibration mode is given by n = 1, 2, 3, ... Equation (5) represents a superposition of normal modes[9] $U_n(x,t)$,

$$U_n(x,t) = (\alpha_n \cos(n\pi t) + \beta_n \sin(n\pi t))\sin(n\pi t). \tag{5}$$

In terms of physical variables, the normal modes are depicted with the following equation:

$$U_n'(x',t') = \left(\alpha_n \cos\left(\frac{n\pi c}{l}t'\right) + \beta_n \sin\left(\frac{n\pi c}{l}t'\right)\right)\sin\left(\frac{n\pi x'}{l}t'\right). \quad (6)$$

The periodic function for a real number T is given as

$$f(t+T) = f(t), \quad (7)$$

where t is a measure of time in both physical or dimensionless. Therefore, $f(t)$ has T period with same dimensions of time. The period of the individual normal mode $U_n'(x',t')$ is $2/n$ and in physical variables its $2l/nc$, where l represents the wavelength.

The frequency f is defined as $f = 1/T = 1/period$ is a definition of frequency. Each normal mode $U_n'(x',t')$ has a frequency in physical variables with units hertz or cycle/seconds,

$$f_n = \frac{w_n}{2\pi} = \frac{nc}{2l} = \frac{n}{2l}\sqrt{\frac{\tau}{\rho}}. \quad (8)$$

Furthermore, the angular frequency of the impeller is defined as $w = 2\pi f$. Since each mode is characterized with angular frequency $w_n = 2\pi f_n = n\pi c/l$, the normal mode can be re-written with respect to frequency,

$$\begin{aligned} U'_n(x',t') &= \left(\alpha_n \cos\left(\frac{n\pi c}{l}t'\right) + \beta_n \sin\left(\frac{n\pi c}{l}t'\right)\right)\sin\left(\frac{n\pi x'}{l}t'\right) \\ &= \left(\alpha_n \cos\left(2\pi f_n t'\right) + \beta_n \sin\left(2\pi f_n t'\right)\right)\sin\left(\frac{n\pi x'}{l}t'\right) \\ &= \left(\alpha_n \cos\left(w_n t'\right) + \beta_n \sin\left(w_n t'\right)\right)\sin\left(\frac{n\pi x'}{l}t'\right). \end{aligned} \quad (9)$$

The lowest mode of the least frequency represents the first harmonics $U_1(x,t)$. This can be represented as a physical variable $U'_1(x',t')$ or as f_1 (fundamental frequency). The frequencies of higher harmonics are integers and multiples of f_1 and are dependent on the number of blades on both the rotor and stator; $f_n = nf_1$.

III. NUMERICAL COMPUTATIONS AND EXPERIMENTAL METHODS

A. Numerical computations

1. Model description and mesh generation

The hub diameter of AFT used in this investigation is 40 mm. The impeller has a diameter of 219 mm with blade number as three (z = 3). The turbine was designed for a shaft rotation speed (N) of 1450 r/min, with axial gap of 20 mm. There are nine guiding vane blades with design flow rate (Q_d) of 196 l/s, whereas the turbine's specific speed (n_s) is 728.2. Figure 1 depicts a three-dimensional model of the investigated model. All other geometric parameters are summarized in Table I.

The impeller, guide vane, and inlet and outlet pipes make up the computational domain in this work. Creo parametric software was used to model these parts. ANSYS ICEM CFD was used to generate structural grids, which were then transformed to un-structural grids as shown in Fig. 2.

The number of grids determines the precision of the numerical computation. As a result, a thorough examination of grid independence is required. Initially, the AFT's comprehensive grid number under the design condition was calculated using five schemes: 6.6, 7.07, 7.50, 7.89, and 8.11 × 10^6[23] (see Fig. 3). The number of grids determines the precision of the numerical computation. When the total grid numbers of the AFT model is 7.50 × 10^6, grid independence analysis shows that increasing the grid number has minimal influence on head,

$$H = \frac{P_1 - P_2}{\rho g}. \quad (10)$$

Therefore, the total grid numbers of 7.50 × 10^6 (impeller: 2.80 × 10^6, guide vane: 2.30 × 10^6, and inlet 1.3 × 10^6 and outlet pipes: 1.0 × 10^6) were selected in order to improve the reliability of the data as well as reduce the computational workload (see Table II for more details).

2. Governing principles

To numerically analyze the flow field, a turbulent, unstable, and incompressible fluid (water) at 25 °C was used. The fluid flowing through the turbine was solved using a moving reference frame, while the turbine's static flow component was computed using an inertial reference frame. The pressure fluctuation features in the AFT

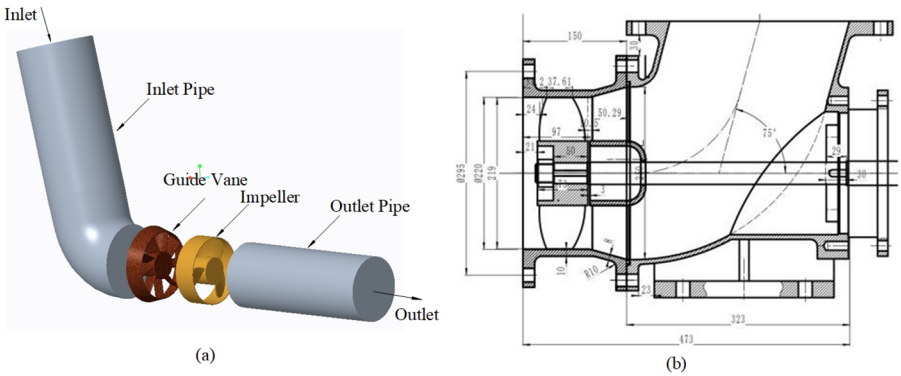

FIG. 1. Geometrical structure of AFT: (a) 3D and (b) 2D.

TABLE I. Investigated turbine specification.

Parameter	Symbol	Quantity (Unit)
Specific speed	n_s	728.2
Design flow rate	Q_d	196 l/s
Rotating speed	N	1450 rpm
Impeller outer diameter	D	119 mm
Impeller hub diameter	d	40 mm
Inlet diameter of guide vane	D_i	250 mm
Outlet diameter of guide vane	D_o	200 mm
Number of impeller blades	z	3
Number of guide vanes	Z_v	9
Tip clearance	t_c	1 mm
Axial clearance	ϑ	20 mm

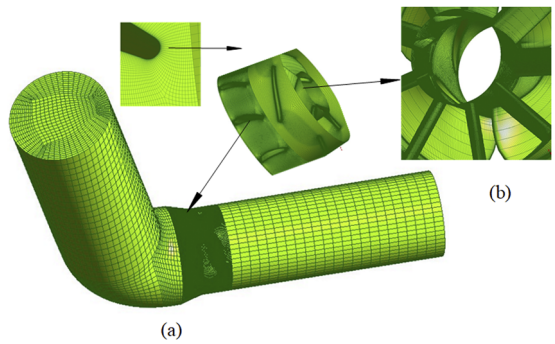

FIG. 2. Computational grid of the AFT: (a) entire turbine and (b) impeller and guide vane assembly.

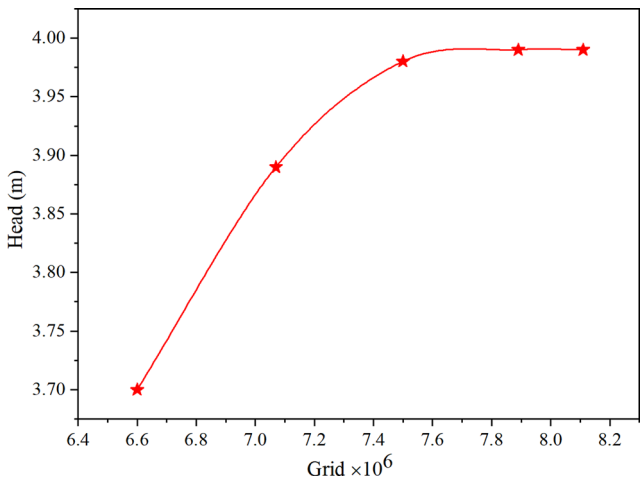

FIG. 3. Grid-sensitivity study.

TABLE II. Grid division.

Components	Grid type	Number
Inlet pipe	Structured	1 318 234
Outlet pipe	Structured	1 101 872
Impeller	Structured	2 801 008
Guide vane	Structured	2 310 083
Total		7 531 197

were analyzed and unraveled using the following continuity and momentum equations:

$$\frac{du_i}{dx_i} = 0, \tag{11}$$

$$\rho\left[\frac{\partial \overline{u_i}}{\partial t} + \frac{\partial(\overline{u_j u_i})}{\partial x_j}\right] = \frac{\partial}{\partial x_j}\left[\mu\left(\frac{\partial \overline{u_i}}{\partial x_j}\right) - \rho\overline{u'_j u'_i}\right] - \frac{\partial \overline{p}}{\partial x_i}. \tag{12}$$

3. Turbulence model

Throughout this investigation, the SST turbulence model is employed to solve flow equations in the AFT. SST is a mixture of the transformed k–ω and k–ε equations that alternates and adjusts between turbine walls and free-flow regions. In details, Menter[24] and Wilcox[25] demonstrated the improvement of the k–ω turbulence model. The blending function for Wilcox model was developed by Menter[24] since it is highly sensitive to free-stream flow by multiplying the k–ω equation by a blending function $F1$, transforming the k–ε equation by $(1 - F1)$. The suitability of SST model for resolving turbulence in AFT was presented by researchers.[26–28] The equations are presented as follows:

TABLE III. Computational domain setup.

Domain location	Boundary type	Mass and momentum
Inlet of inlet pipe	Inlet	Total pressure
Outlet of outlet pipe	Outlet	Opening
Domain surfaces	Wall	No-slip
Turbulence model		
Model applied		Standard SST k-ω
Interface configuration		
Steady-state		Frozen-rotor
Transient-state		Transient rotor–stator
Numerical calculation solver control		
Steady-state		1000 iterations
Timestep		1.15×10^{-4} s
Total time		1.24×10^{-1} s
rms residual target		10^{-5}
Mesh connection		General grid interface (GGI)

k–ω equations:

$$\frac{\partial(\rho k)}{\partial t} + \frac{\partial}{\partial x_j}(\rho U_j k) = \frac{\partial}{\partial x_j}\left[\left(\mu + \frac{\mu_t}{\sigma_{k1}}\right)\frac{\partial k}{\partial x_j}\right] + P_k - \beta'\rho k\omega, \quad (13)$$

$$\frac{\partial(\rho\omega)}{\partial t} + \frac{\partial}{\partial x_j}(\rho U_j \omega) = \frac{\partial}{\partial x_j}\left[\left(\mu + \frac{\mu_t}{\sigma_{\omega 1}}\right)\frac{\partial \omega}{\partial x_j}\right] + \alpha_1 \frac{\omega}{k} P_k - \beta_1 \rho\omega^2. \quad (14)$$

Transformed *k–ε* model:

$$\frac{\partial(\rho k)}{\partial t} + \frac{\partial}{\partial x_j}(\rho U_j k) = \frac{\partial}{\partial x_j}\left[\left(\mu + \frac{\mu_t}{\sigma_{k2}}\right)\frac{\partial k}{\partial x_j}\right] + P_k - \beta'\rho k\omega, \quad (15)$$

$$\frac{\partial(\rho\omega)}{\partial t} + \frac{\partial}{\partial x_j}(\rho U_j \omega) = \frac{\partial}{\partial x_j}\left[\left(\mu + \frac{\mu_t}{\sigma_{\omega 2}}\right)\frac{\partial \omega}{\partial x_j}\right] + 2(1 - F_1)\rho\frac{1}{\sigma_{\omega 2}\omega} \times \frac{\partial k}{\partial x_j}\frac{\partial \omega}{\partial x_j} + \alpha_2 \frac{\omega}{k} P_k - \beta_2 \rho\omega^2. \quad (16)$$

F_1 and F_2, as presented in Eqs. (8) and (9), represent blending functions,

$$F_1 = \tanh(\Gamma_1{}^4), \quad (17)$$

$$F_2 = \tanh(\Gamma_2{}^2). \quad (18)$$

The turbulence viscosity, μ_t, is computed with the following equation:

$$\mu_t = \frac{\alpha_1 k\rho}{\max(\alpha_1\omega, SF_2)}. \quad (19)$$

The *k–ω* equation applied to aid the prediction of the internal wall layers was accompanied by coefficients—σ_{k1} = 1.176, $\sigma_{\omega 1}$ = 2.0, $\beta 1$ = 0.075, α_1 = 5/9, β' = 0.09 while σ_{k2} = 1.0, $\sigma_{\omega 2}$ = 1/0.856, and β_2 = 0.828—applied along the free-stream.[29]

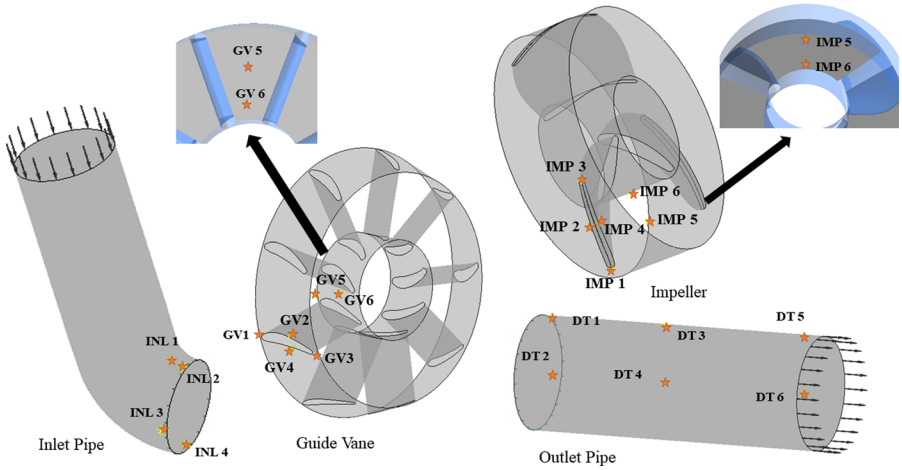

FIG. 4. Location of pressure monitoring points.

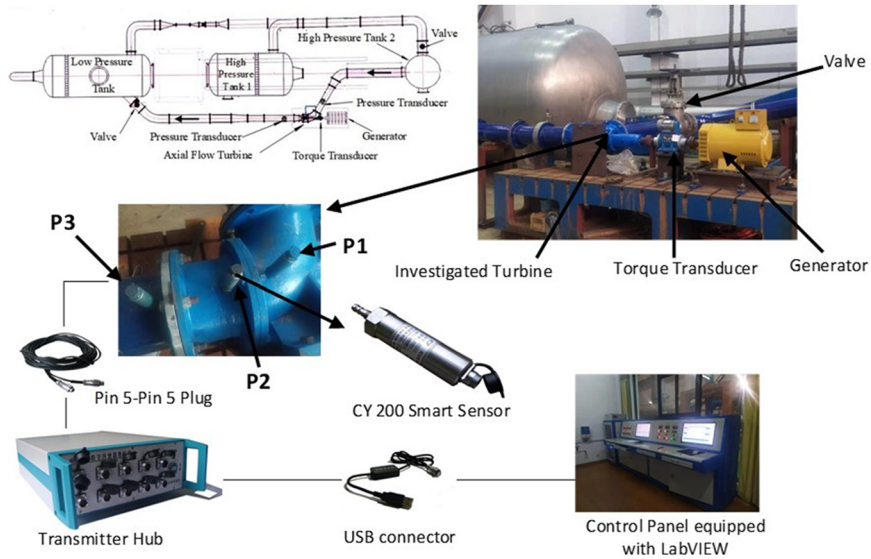

FIG. 5. Schematic diagram of the closed test rig.

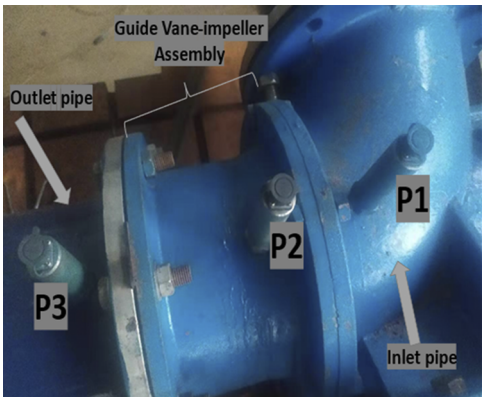

FIG. 6. The location of pressure sensors.

4. Boundary condition setup

The complicated nature of flow patterns within the domain of an AFT calls for a suitable turbulent model for accurate prediction of its interior flow behavior. To meet this requirement, the standard SST *k–w* model was selected using ANSYS CFX commercial software to resolve 3D unsteady Reynolds-averaged Navier–Stokes (RANS) equation. The numerical computation for the steady state was executed by applying frozen rotor interphase to compute the flow at the impeller's interphase. The flow is normally positioned to the boundary, and as a result, a total pressure of 1000 Pa, reference pressure of 1 atm, and 5% turbulence intensity were applied. Interior wall configuration of no-slip was applied. In order to ensure there is no conflict between non-matching cells since different pitch angles is unavoidable, the general grid interphase (GGI) is applied to the mesh. Steady-state calculations were not sufficient to divulge flow characteristics in the turbine after 1000 iterations. Consequently, the steady state result was utilized to initiate the unsteady-state computations where the transient rotor–stator selected at the rotating impeller surface updates the positions at every timestep. A timestep of 1.15×10^{-4} s, representing impeller rotation of 1°, was used since it is suitable enough to extract the essential time resolution. Three complete impeller revolutions were considered, resulting in total time of 1.24×10^{-1} s. To accurately discretize time, the backward second order Euler scheme was applied along with ten (10) maximum flow iterations per timestep. In addition, root mean square (rms) was selected using a specific target of 10^{-5}. A summary of the setup is presented in Table III.

5. Description of monitoring points

As shown in Fig. 4, the pressure-flow characteristics were monitored throughout the flow region. Monitoring points at the inlet pipe are referred to as "INL." Similarly, "GV," "IMP," and "DT" stand for guiding vane, impeller, and output pipe monitoring points, respectively.

B. Experimental method

An unsteady state pressure fluctuation intensity test of the turbine on a laboratory-scale was carried on the four-quadrant hydraulic test rig at Jiangsu University, as shown in Fig. 5.

The four-quadrant operation test rig meets both International standard ISO9906 and Chinese national standards and duly certified by the technological department of Jiangsu province. The overall permissible uncertainty of tested efficiency is ±0.3%.

The turbine device was installed with a generator connected to the shaft in order to provide the power output from the tested turbine device. To monitor shaft speed and power, a JCL2/500 Nm torque meter with an accuracy of ±0.1% was mounted between the shaft and the motor. The shaft is coupled with the hub of the impeller as torque is transmitted from the impeller to the shaft, thereby turning the generator to produce electrical energy. To keep the flow and water pressure consistent, the inlet and outlet pipes were linked to the inlet and outlet water tanks, respectively. When the head of the tested device is low, a booster pump was connected to the outlet pipe to improve the flow rate. Pressure valves are used to control pressure drops and operating conditions in the test loop. The flow rate was recorded using an electromagnetic flowmeter with a ±0.2% error. To measure the head of the turbine during the test, an EJA 110A intelligent differential pressure gauge with a test range of 0–25 m and an uncertainty of ±0.1% was connected to the inlet and exit water tanks. The pressure pulsation intensity was acquired by installing three dynamic pressure transducers (CY200) with overall precision of 0.1%, at the inlet (P1), guide vane (P2), and outlet pipe (P3), as presented in Fig. 6.

By making full use of the microprocessor's processing and storage capacity, the CY200 integrates a piezoresistive silicon crystal and a single-chip microcomputer system and realizes the filtering, amplification, A/D conversion, correction, and other functions of the pressure signal picked up by sensitive components. On the linked computer, the recorded pressure signal is directly presented as

TABLE IV. Test equipment and related parameters.

Test parameters	Measuring instrument	Type	Measuring range	Calibration Accuracy (%)
Rotating speed	Digital torque speed indicator	JW5624	⋯	±0.1
Torque	Speed torque sensors	JCL1	200 Nm	±0.1
Flow rate	Electromagnetic flowmeter	German cologne intelligent electromagnetic	0–1000 l/s	±0.2
Head	Differential pressure transmitter	EJA530E	0–60 m	±0.1
Pressure fluctuation	Smart pressure sensor	CY200		±0.1

digital signals and stored for subsequent study. A sampling frequency fs and period of 1000 Hz and 20 s, respectively, were observed after the turbine attains stable operating condition. The frequency analysis falls within the requirements of Nyquist sampling theorem range of 0–441.7 Hz. The test equipment and their related parameters are summarized in Table IV.

IV. RESULTS AND DISCUSSIONS

A. Comparison of pressure pulsation of experiment test and CFD

The pressure pulsating coefficient (C_p) was computed on all grids within the turbine's flow domain by statistical means to

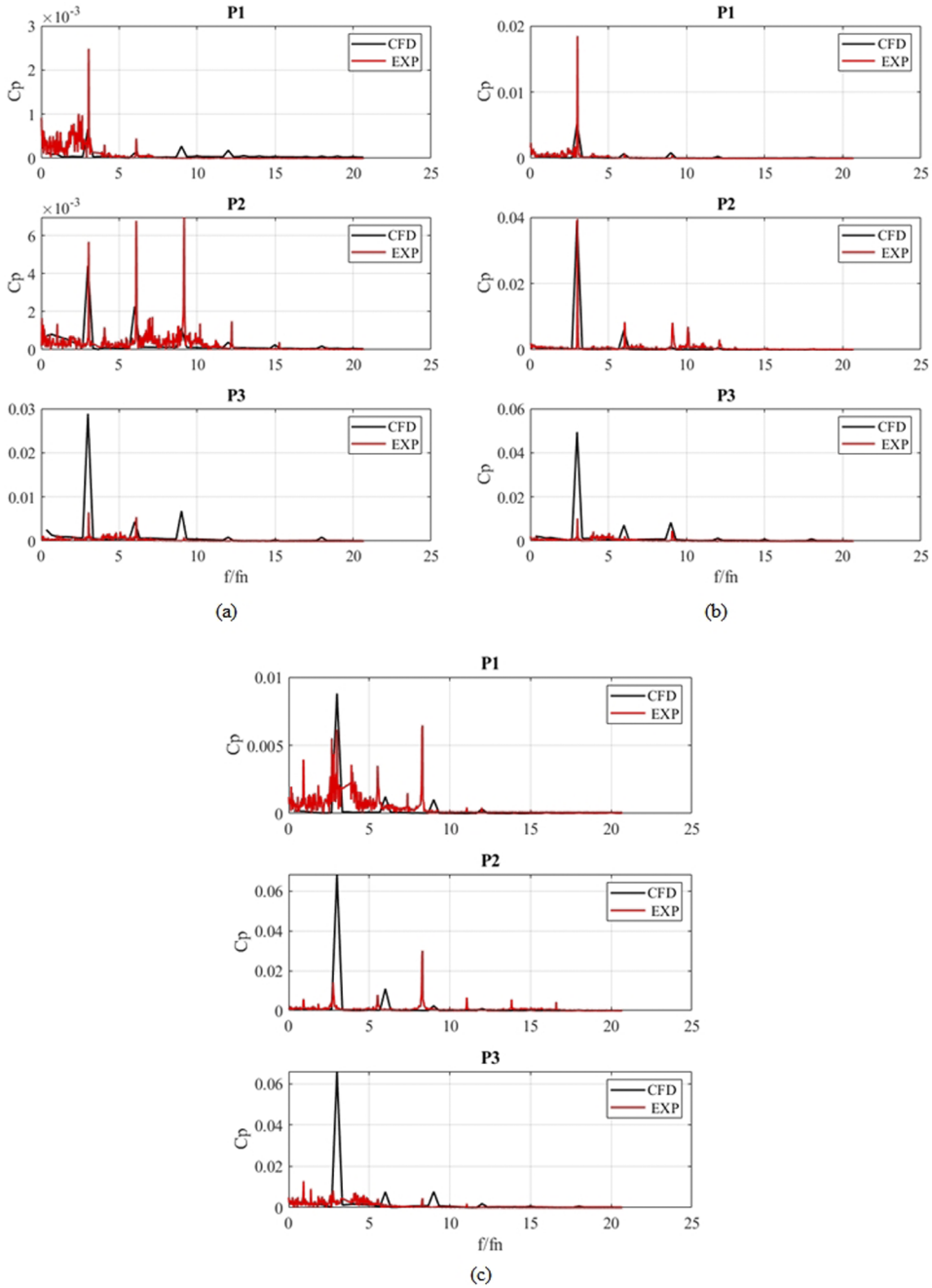

FIG. 7. Comparison of computational and experimental frequency-domain: (a) $0.8Q_d$, (b) $1.0Q_d$, and (c) $1.3Q_d$.

facilitate the characterization of the regions associated with extremely unsteady and transient flows in order to comprehensively analyze the pressure fluctuation in the axial-flow turbine. Instantaneous pressure, p, at specific nodes is disintegrated into two pressure components: the periodic pressure variable, p, represents the pressure component produced due to periodic change in the blade passing frequency (BPF), and the averaged-time variable, p. The dimensionless coefficient of pressure C_p is evaluated using Eq. (20) to outline the periodic pressure in relation to time and the angle of rotation of the impeller,

$$C_p = \frac{\left(P(no\,\mathrm{de,t}) - P_{ref}\right)}{\frac{1}{2}\rho U_2^2}. \tag{20}$$

Furthermore, experimental test was carried out to verify the CFD results and to reveal the pressure fluctuations at the inlet, guide vane, and outlet pipe corresponding to pressure sensor points P1, P2, and P3, respectively (see Fig. 6).

The pressure sensors were connected to a transmitter hub and control panel, as presented in Fig. 5. The pneumatic valves were opened from the control panel to the desired flow rate, and the pressure signals were recorded. The above procedure was repeated for different flow rates with their corresponding time-domain pressure pulsations signals recorded. Furthermore, FFT technique was applied to the time domain signals obtained from both experimental test, and CFD values after the pressures were normalized by means of Eq. (20). Figure 11 depicts the frequency-domain history of the pressure intensity (C_p) for both experimental and CFD at $0.8Q_d$, $1.0Q_d$, and $1.3Q_d$ for the three sensors P1, P2, and P3. The experimental values are in fair agreement with CFD results but with slight variation. The main frequencies of the CFD agree with the experimental values, but the experimental values are above CFD at $0.8Q_d$ and $1.0Q_d$ at P1, as shown in Figs. 7(a) and 7(b).

Under all flow design conditions, the experimental test at sensors (P1, P2, and P3) reveals that the main amplitude of C_p increases with the increase in flow rate. Second, the numerical simulation and experimental test results of the pressure pulsation in the turbine are consistent near the blade frequency, but the deviation is more significant at higher frequencies. The above discrepancies can be attributed to the turbine vibration during the model test, which increases the complexity of the flow interactions in the turbine. In general, there is a quantitative agreement between the experimental and CFD values, thereby establishing the CFD computation suitable for further analysis on other monitoring points in the turbine.

B. Time domain analysis of pressure pulsation

The pressure fluctuation of the turbine is caused by the interaction between the rotor and the stator.[11] However, to explore the pressure field intensity, transient simulation was executed at $0.8Q_d$, $1.0Q_d$, and $1.3Q_d$ using a shaft speed of 1450 r/min. Furthermore, the various C_p at different monitoring points in the inlet, guide vane, impeller, and outlet pipes were analyzed and presented.

1. Inlet flow passage

Figure 8 shows the time domain history of C_p in the intake pipe for one impeller revolution. The graphs show the periodic variation in C_p with respect to timestep, which corresponds to the impeller's degree position.

Three peaks and troughs were detected in the turbine during one complete impeller rotation, which reflect the number of blade passages per shaft revolution. The impeller's rotation causes blade passing over the monitoring points, resulting in a pressure differential between high- and low-pressure zones. The lowest and highest C_p values were found at "INL1" and "INL4," respectively. Due to the variables utilized in determining C_p in Eq. (11), the severity of pressure fluctuation rises when flow rate increases from $0.8Q_d$ to $1.3Q_d$.

2. Guide vane flow passage

Figure 9 depicts a one-revolution time-domain history of C_p in the guiding vane at monitoring points GV1 to GV6. Because of their geometric proximity to the vane region, monitoring points "GV1"

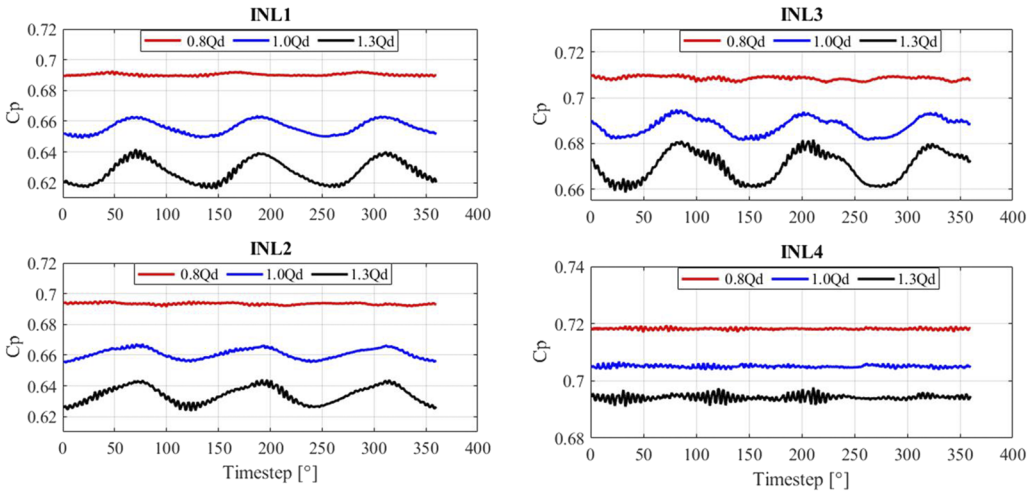

FIG. 8. Time-domain history of C_p within the inlet pipe.

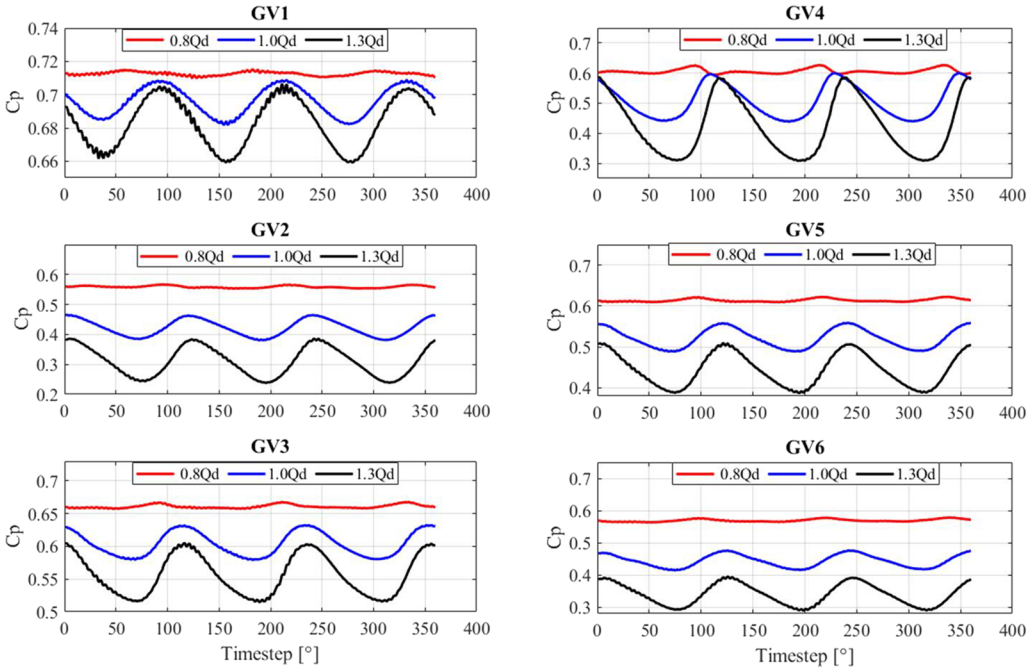

FIG. 9. Time-domain history of C_p within the guide vane.

and "GV4" recorded the maximum amplitude. Furthermore, C_p values were lowest in GV2 and GV6. Due to its closeness to the impeller, GV3 saw the most pulsations. Peak-to-peak C_p falls as flow rate increases from $0.8Q_d$ to $1.0Q_d$ to $1.3Q_d$. Across all flow conditions, the lowest C_p value was obtained at "GV2."

3. Impeller flow passage

Figure 10 shows the time-domain history of C_p for one impeller rotation at six distinct locations, from "IMP1" to "IMP6." Nine uneven peaks and valleys, matching to the guide vanes' blades, were recorded while the impeller rotated through 360°. As each monitoring point on the spinning impeller sweeps through the nine blades of the guide vane in one shaft rotation, it is a clear depiction of the stator blades' influence. This demonstrates how the rotor–stator interaction between the stationary guide vane and revolving impeller affects C_p within the impeller.[7,9]

As the fluid travels from the impeller's leading edge (LE) at "IMP1" to the impeller's trailing edge (TE) at "IMP3," the C_p drops. The energy transfer from the fluid to mechanical energy in the form of shaft rotation is responsible for the decrease in C_p. C_p decreases somewhat at the blade suction surface (IMP 4), but increases again at "IMP5" and "IMP6," which are positioned within the impeller's cascade. IMP1 had the greatest C_p values for $0.8Q_d$ and $1.0Q_d$, but it was lower than IMP2's C_p values for $1.3Q_d$. Furthermore, the high velocity of fluid exiting the guide vane impinges heavily on the impeller's leading edge (LE), resulting in a complex, varied flow interaction, and, as a result, a high C_p. Furthermore, because IMP2 is situated on the impeller's PS, the C_p values recorded by it are high for all flow conditions. With an increase in flow from $0.8Q_d$ to $1.3Q_d$, the C_p decreases across all monitoring locations.

4. Outlet pipe flow passage

Figure 11 depicts the C_p in the outlet pipe during a full revolution. The outlet pipe domain had six monitoring points, numbered "DT1" through "DT6." The pulses measured at "DT1" are the most pulsating of all the monitoring locations (DT2 to DT6) because of its closeness to the impeller blade tip exit. Nine peaks and troughs were recorded from "DT2" to "DT6," corresponding to the number of blades on the guiding vane. As the fluid exits the outlet at "DT5" and "DT6," the amplitude of the C_p progressively diminishes. C_p values drop from the wall area at "DT1," "DT3," and "DT5" to the outlet pipe center at "DT2," "DT4," and "DT6." Pressure pulsation diminishes as the distance between the monitoring points and the impeller increases, as seen by the decreasing C_p trend within the output pipe from DT1 to DT6. C_p in the output pipe had the lowest fluctuation across all flow conditions.

5. Pressure pulsation strength

The pressure pulsation strength for all the monitoring points across the flow conditions was evaluated using Eq. (21) and compared as shown in Fig. 12. At the inlet flow domain, the signal strength was found to reduce gradually from $0.8Q_d$ to $1.3Q_d$. A similar trend was observed in the guide vane flow domain. In Fig. 12(c), irregular pressure pulsation strength pattern was recorded. At IMP1, the pressure pulsation strength increased from 0.75 at $0.8Q_d$ to 0.77 at $1.0Q_d$, but fell drastically at $1.3Q_d$. Furthermore, irregular pressure pulsation strengths were registered in the outlet pipe,

$$I_{C_p} = \left[\frac{\sum {C_p}^2 \times \Delta t}{T}\right]^{1/2}. \tag{21}$$

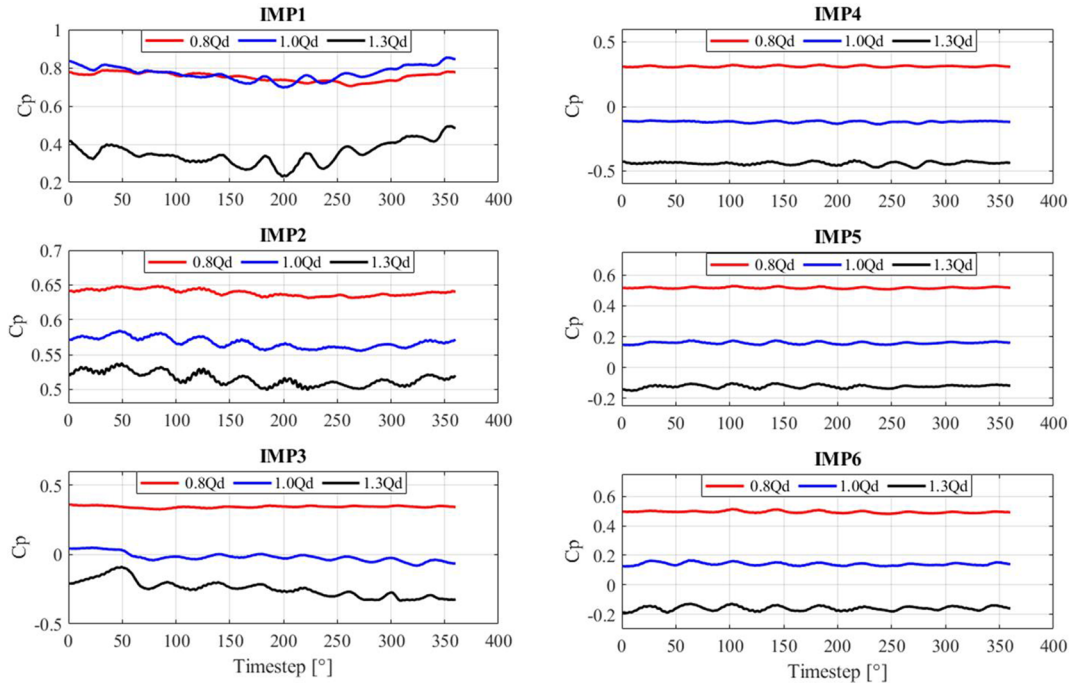

FIG. 10. Time-domain of C_p within the impeller.

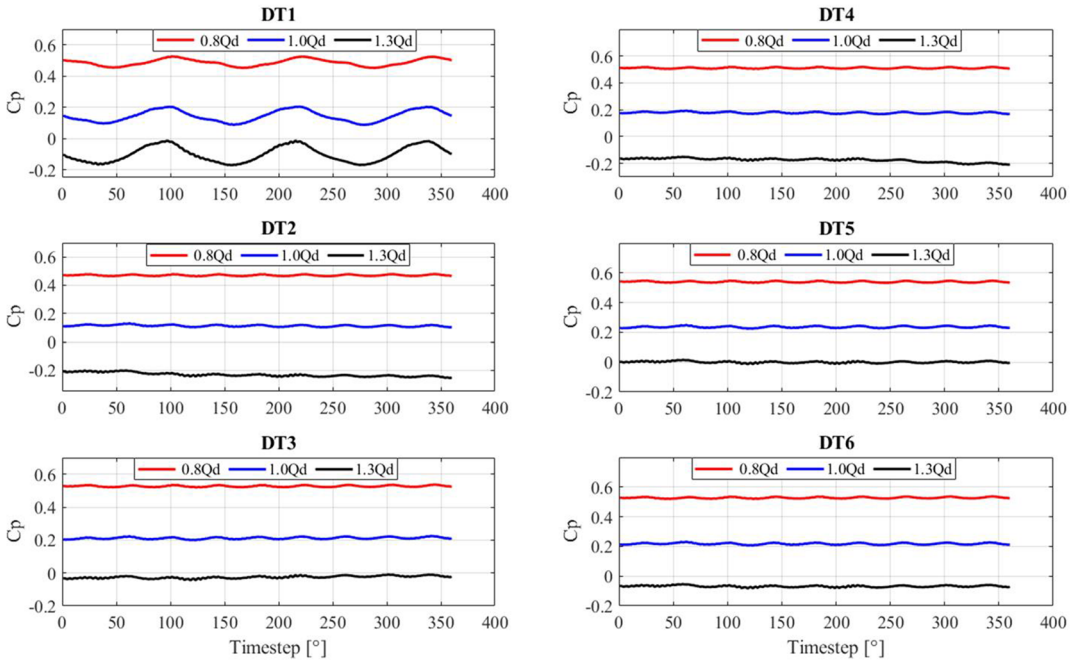

FIG. 11. Time-domain of C_p at within the outlet pipe.

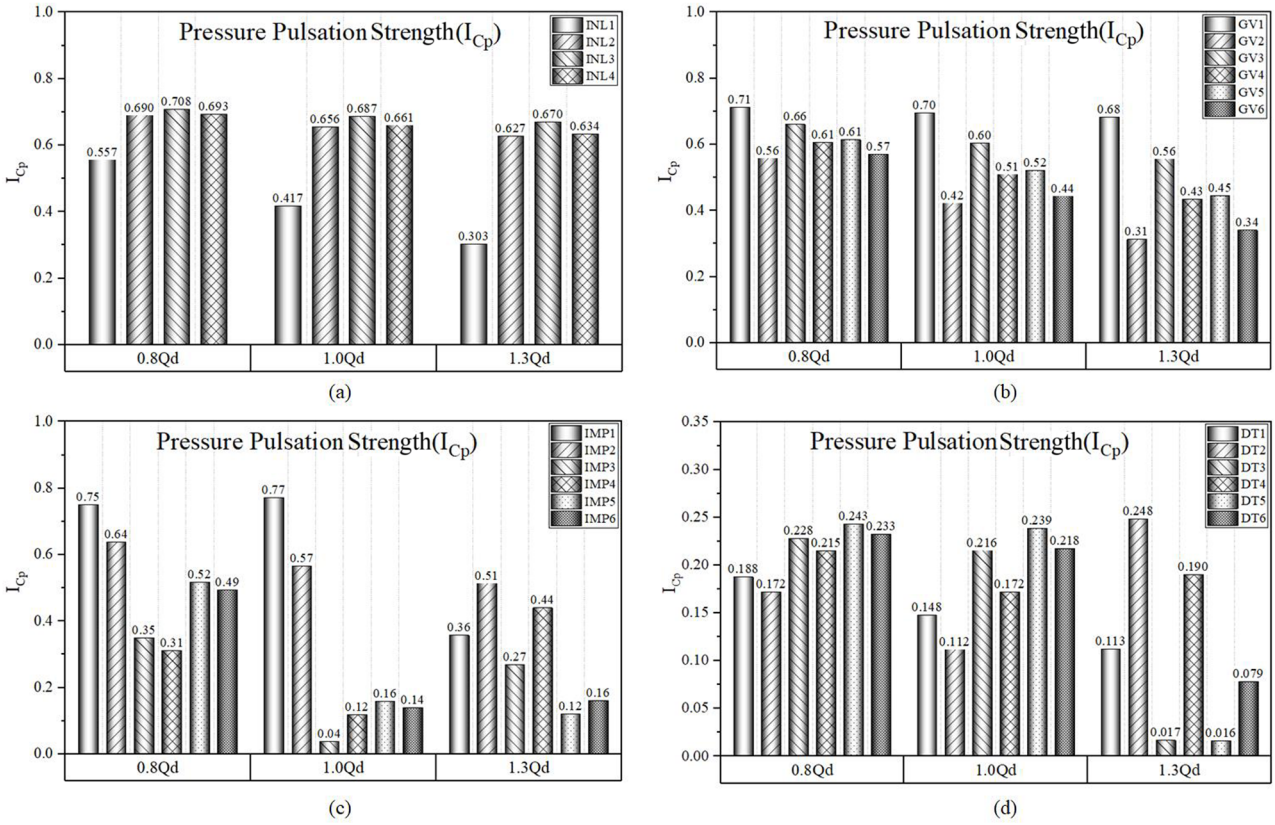

FIG. 12. Pressure pulsation strength across all monitoring points. (a) Inlet, (b) guide vane, (c) impeller, and (d) outlet pipe.

C. Frequency-domain history of the pressure pulsations in the AFT

1. Inlet pipe flow passage

The fast Fourier transformation (FFT) was used to get the unsteady frequency-domain history of the turbine, as shown in Fig. 13. The rotational frequency is 24.1667 Hz since the turbine was operated at a speed of 1450 rev/m. Excitation frequencies of $3f_n$, $6f_n$, and $9f_n$ were marked for the first three excitation frequencies. The flow exchange between the guide vane and the impeller, which is controlled by the impeller blade number, was revealed to be the cause of harmonic excitation.

The transient and unstable components in pressure pulsation signals were analyzed using the time–frequency domain as shown in Fig. 14 for the four monitoring points in the inlet pipe flow domain. The peak amplitude was recorded at 72.50 Hz, which corresponds to the blade passing frequency (BPF = $3f_n$). The increase in flow rate leads to the increase in amplitude of C_p across all monitoring points in the inlet flow passage.

2. Guide vane flow passage

Figure 15 shows the turbine's unsteady frequency-domain history calculated using FFT. $3f_n$, $6f_n$, and $9f_n$ are the first three excitation frequencies. The excitation effect due to harmonics recorded across all the monitoring points is the consequences of flow exchange between the guide vane and the impeller, which is dependent on blade number. The amplitude was found to increase with the increase in flow rate across all flow conditions.

The joint time frequency-domain history of C_p in the guide vane is similar to the pattern observed at the inlet pipe. Large discontinues amplitude of C_p were recorded between 70 and 73 Hz, as shown in Fig. 16. Furthermore, the amplitude increases with increase in flow rate.

3. Impeller flow passage

Figure 17 depicts the turbine's unstable frequency domain history calculated by FFT. The mean frequency is 24.1667 Hz, due to the shaft rotation speed of 1450 rev/min. The blade passing frequencies occurred at $9f_n$, $18f_n$, and $27f_n$, which corresponds to the number of vanes on the guiding vane. The guiding vane's influence was found to be dominating on all of the impeller's monitoring points.

In Fig. 18, the time–frequency reveals the irregular and unsteady pulses recorded across the impeller's monitoring points. The shaft rotating frequency was discontinuous, resulting in pressure fluctuations of the main frequency. The impeller blades are susceptible to irregular fluid forces with varying frequencies. The bearings and blades of the impeller are susceptible to fatigue, which

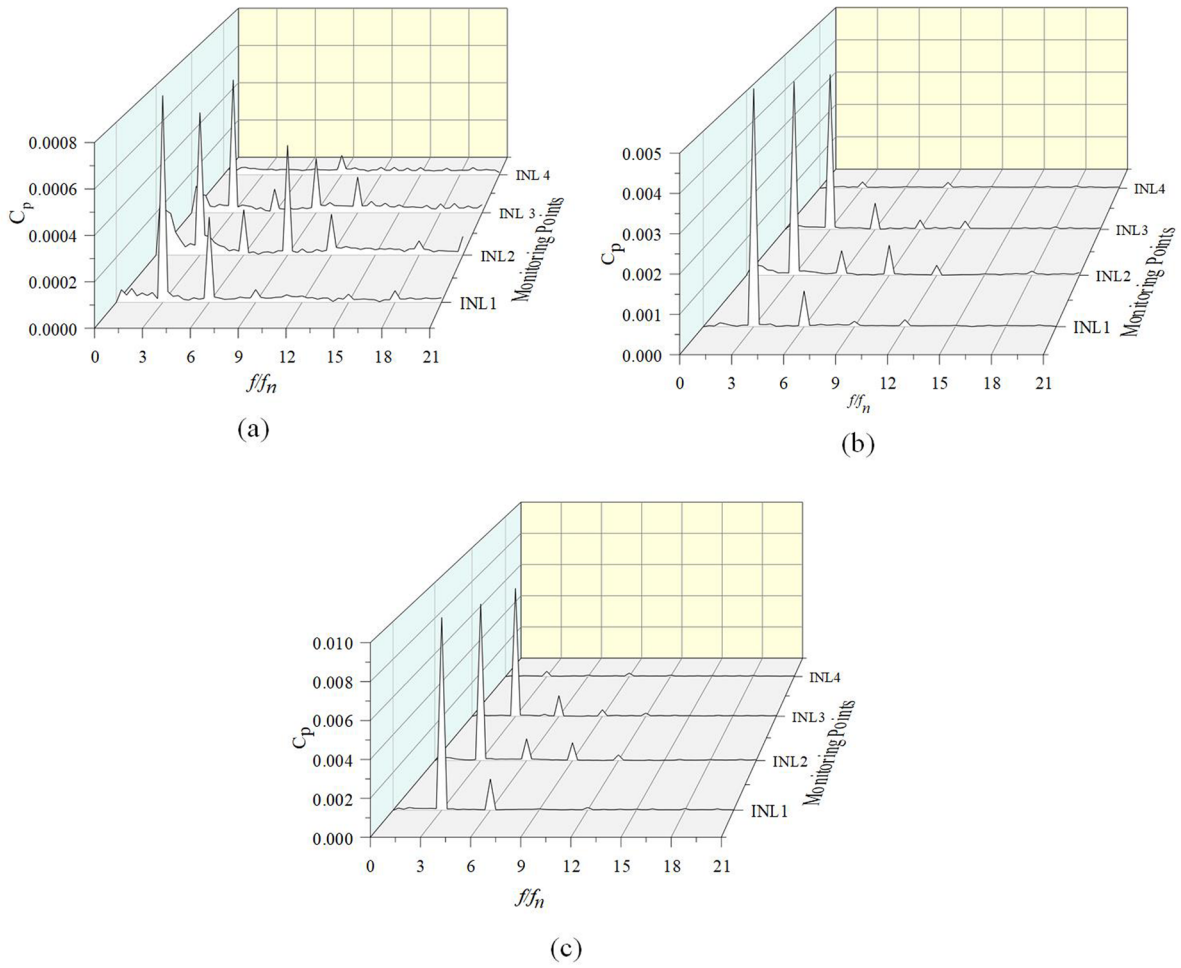

FIG. 13. Frequency-domain of C_p within the inlet pipe. (a) $0.8Q_d$, (b) $1.0Q_d$, and (c) $1.3Q_d$.

affects stability and life span of the turbine under varying load condition.

4. Outlet pipe flow passage

The frequency-domain of the C_p for all monitoring points (DT1 to DT6) in the output pipe is shown in Fig. 19. The frequency within the output pipe is a result of the combined effects of the guide vane and impeller. The excited main frequencies of Cp across the inlet pipe and guide vane were observed at DT1 at the outlet pipe. Also, for the other monitoring points (DT 2 to DT 6), the excited main frequencies observed on the impeller were recorded. The excitation effect caused by harmonics was discovered to be the result of flow exchange between the guide vane and the impeller, which is influenced by the number of blades on both the guide vane and the impeller. The C_p amplitude of "DT1" to "DT6" gradually declines with an increase in excitation frequency. As presented in Fig. 19, C_p in the outlet pipe depicts the spread of pressure pulses resulting from the interaction of the rotor (impeller) and stator (guide vane).

The joint time–frequency domain of the C_p in the outlet pipe reveals two separate patterns as presented in Fig. 20. Similar frequency patterns observed in the inlet pipe and guide vane were visible at DT1, whereas DT2 to DT 6 recorded main frequencies and harmonics similar to those observed at the impeller flow passage.

D. Influence of impeller–guide vane interaction on periodic pressure pulsation

The runner's rotation in relation to the guide vane causes a variety of periodic phenomena to occur, which are overlaid on the average fluid velocity and pressure in the fluid channels. They appear as single frequencies in the pressure spectra due to their periodic character, which is generated by any slight fluctuation in rotating speed, as described in Secs. IV B and IV C. If the frequency of the precisely periodic excitation corresponds with a sufficient natural mode of the structure, unwanted resonating vibration becomes conceivable. The events associated with the blade passage are frequently heard as noise because of their high frequency. Various types of

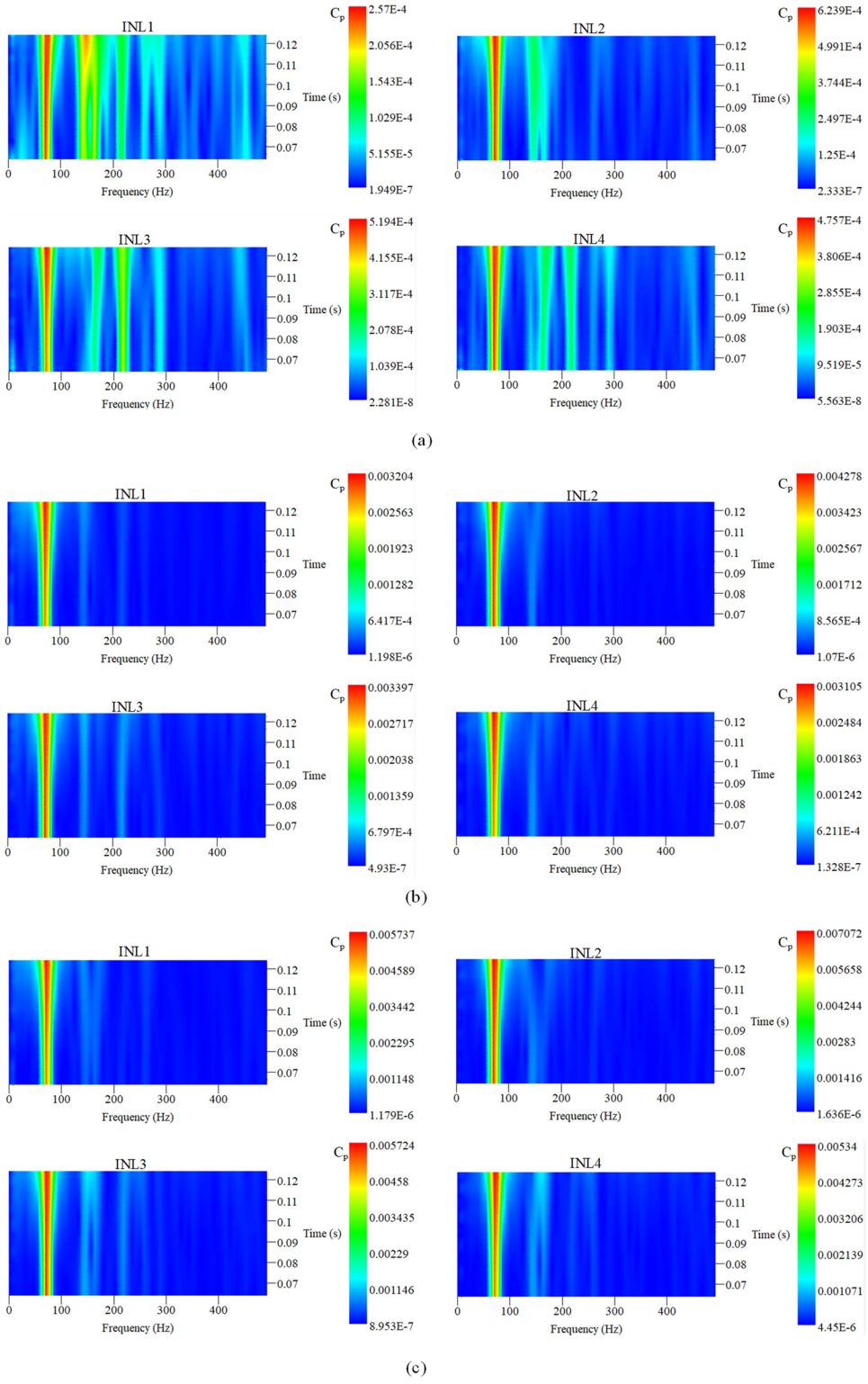

FIG. 14. Time–frequency domain of C_p within the inlet pipe. (a) $0.8Q_d$, (b) $1.0Q_d$, and (c) $1.3Q_d$.

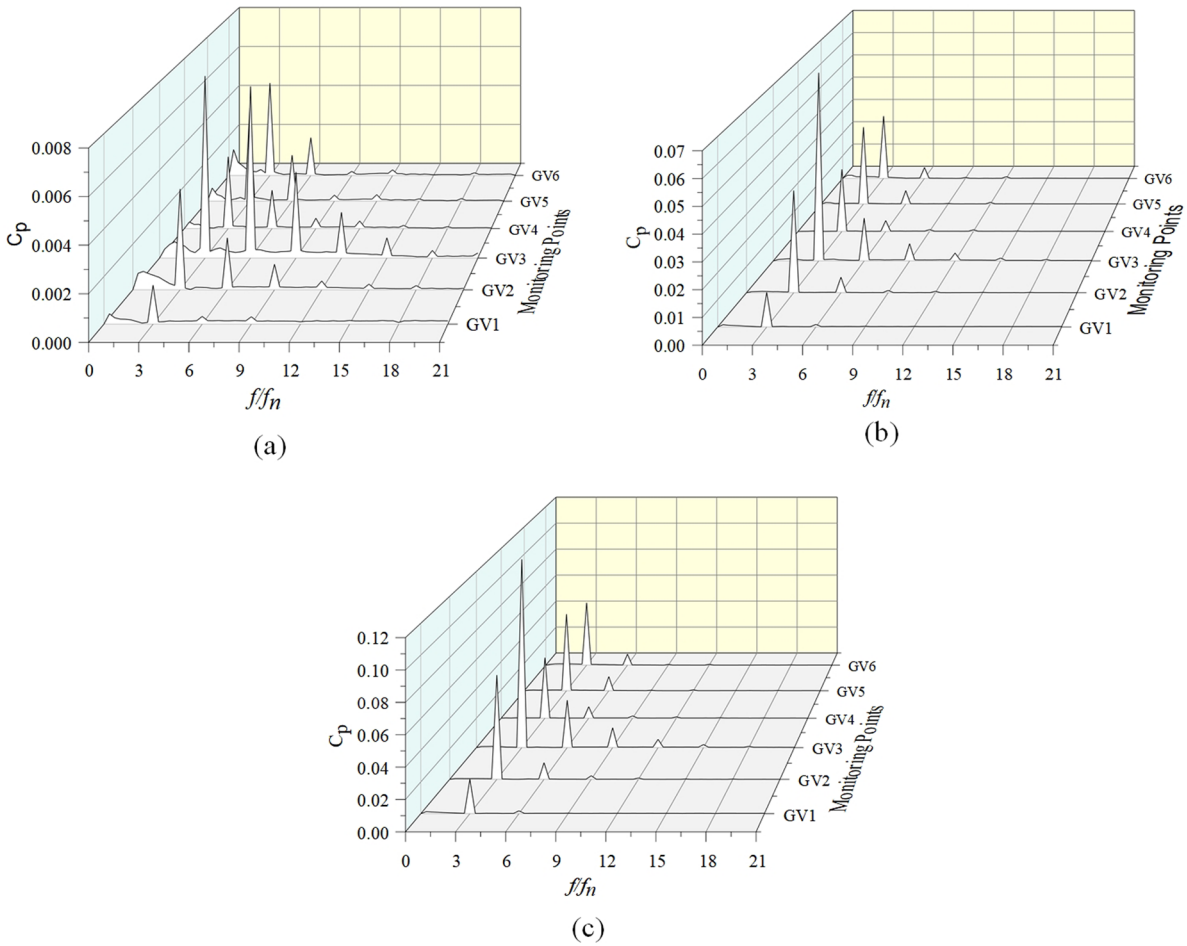

FIG. 15. Frequency-domain of C_p within the guide vane. (a) $0.8Q_d$, (b) $1.0Q_d$, and (c) $1.3Q_d$.

vibration may be induced directly in these flow structures, depending on the blade number in the stationary and rotating cascades. In the guide vane case, unfavorable wave timing might occasionally reveal extra characteristics. Blade-frequency vibration is utilized for vibration diagnostics and plays a significant part in the vibration signature of all types of hydraulic turbo-machines. The effects of rotor–stator interaction can be easily distinguished from flow instabilities using frequency analysis with appropriate precision due to the modest change in runner speed. The periodic effects of a runner rotating at constant speed close to the guide vane (stator) have certain general features that are analyzed first to help comprehend the specific phenomena covered in this section. The revolving and stationary blade cascades of the AFT must be taken into consideration; however, asymmetric characteristics of their geometry, such as the influence of the nose vane in a spiral casing, may be comprehended if they are represented as the limit case of simply one period per rotation (see Sec. IV B). The periodic pulsations revealed three peak to peak pulsations in the guide vane, inlet pipe, and outlet pipe, but at the impeller, nine irregular peak to peak pulses were encountered. The only exceptions were INL4 and DT1 where the signals appear to be a mixture of both the guide vane and impeller blade effect, as would be explained in Sec. IV D 1.

1. Stationary flow domain

The combination of an impeller with z blades and a stationary cascade (guide vane) with Z_{gv} vanes is required to excite a certain pattern of impeller vibration. The inter-relationship between these two cascades is characterized by an exchange of periodic reaction forces whose time variation consists of a fundamental frequency and certain harmonics corresponding to the rotating speed and the blade number in each cascade. Using N as the runner's rotating speed (rev/s), the impact of the impeller's blade on any specific location in the stationary parts (i.e., inlet and outflow pipes included) comprises of the frequencies ($f_{s,k}$) as presented as follows:

$$f_{s,k} = N \times z \times k \quad (k = 1, 2, 3, \ldots). \tag{22}$$

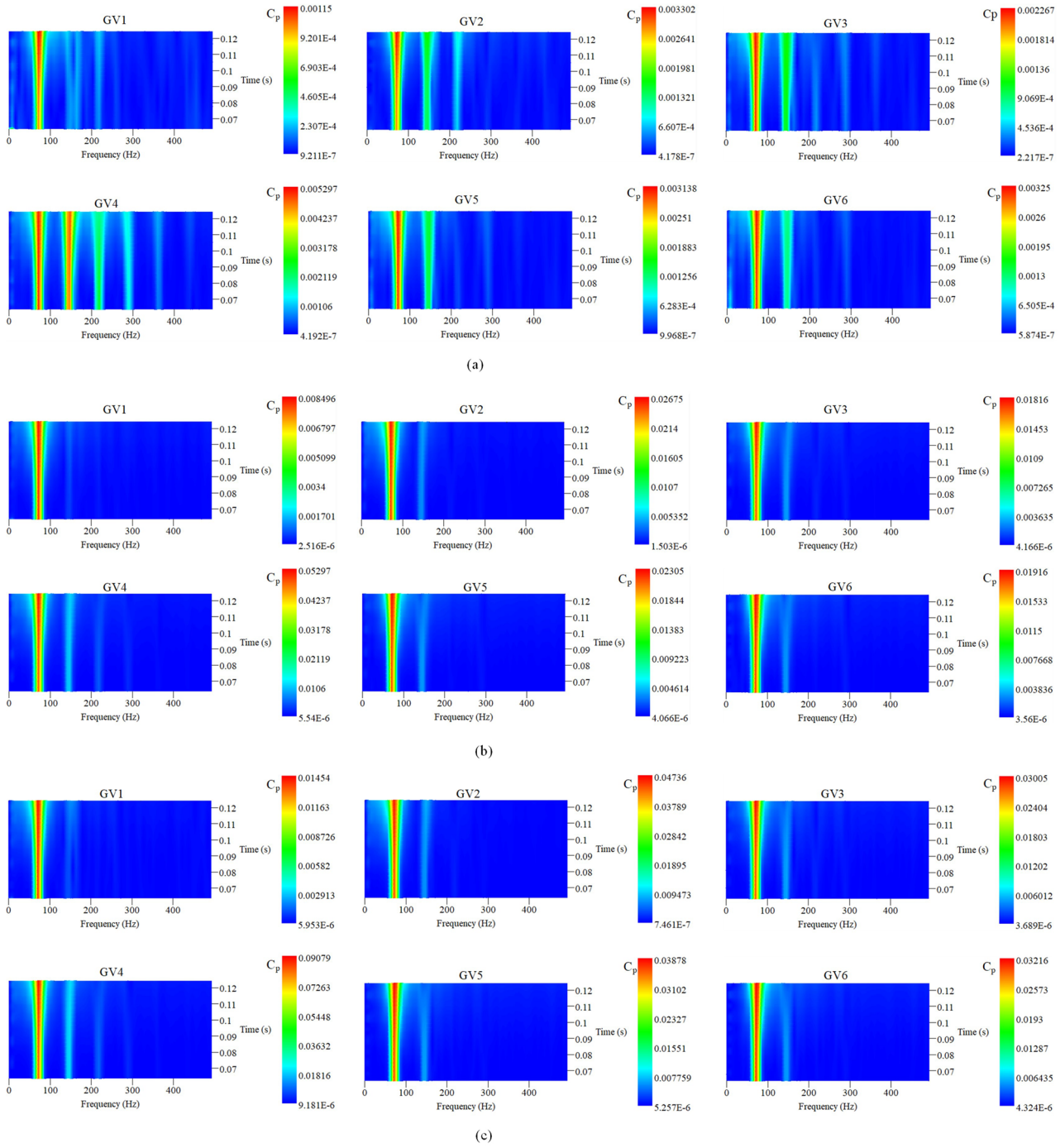

FIG. 16. Time–frequency domain of C_p within the guide vane. (a) $0.8Q_d$, (b) $1.0Q_d$, and (c) $1.3Q_d$.

The lowest of these, when $k = 1$, $N \cdot z$, is the blade passing frequency (BPF) and k is the harmonic number. Since the shaft speed is 1450 rpm/60 = 24.1667 Hz (revolutions per seconds), BPF is $3 \times f_s$, while the first three excitation frequencies occurred at 72.50 Hz ($3 \times f_n$), 145.00 Hz ($6 \times f_n$), and 217.50 Hz ($9 \times f_n$).

The only exception to the above was observed in the outlet pipe flow section. Whenever an AFT blade sweeps over the monitoring

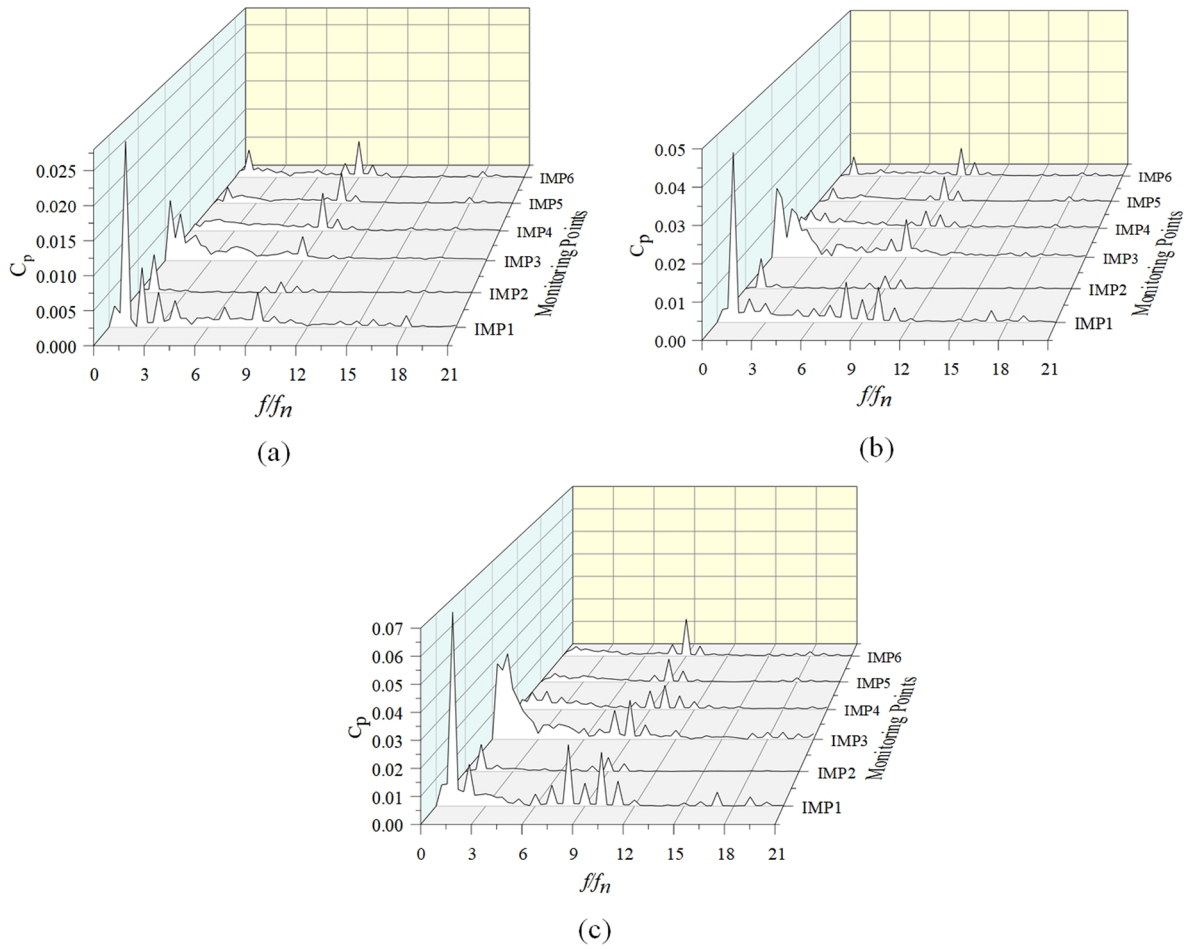

FIG. 17. Frequency-domain of C_p within the impeller. (a) 0.8Qd, (b) 1.0Qd, and (c) 1.3Qd.

points in the outlet pipe, it generates fluctuation in pressure as a result of the differential pressure between the PS and SS of the blade. Dynamic displacement is radially created in the outlet pipe close to DT1, as a result of pressure fluctuations. The C_p plots in time and frequency domain for DT1 (see Fig. 11) reveal this effect as it differs completely from other monitoring points within the outlet pipe. The above scenario is relatively inevitable since the pressure difference across the blade is source of the driving torque for the AFT. The amplitude of C_p steeply decreases with increasing distance from the impeller as presented in Fig. 21(d).

2. Rotating flow domain

The impeller is the sole spinning domain in the AFT. As a continuation of the frequency analysis in Sec. IV D 1, every component (for example, all monitoring points on the blade tip) at the impeller encounters a periodic force from the static guiding vanes at the frequencies $f_{r,m}$ as presented in the following equation:

$$f_{r,m} = N \times Z_{gv} \times m \quad (m = 1, 2, 3, \ldots). \tag{23}$$

The phase of influence of the runner on the ensemble of guiding vanes is not uniform across the runner's perimeter as shown by the impeller monitoring points (IMP1 and IMP3) in Fig. 10. The runner is exposed to a pressure pattern of equal phase sectors separated by nodal diameter, depending on which harmonics (k, m) of the interaction are assessed.

The frequency domain history of the AFT at 1.0Qd is presented in Fig. 20. Based on the excitation trends observed in the stationary system, "m" is positive and is consistent with the impeller rotation. The shaft speed is 1450 rpm/60 = 24.1667 Hz (revolutions per seconds).

Therefore, nine (9) regular peaks and valleys of pressure purses corresponding to the nine vanes on the guide vane were recorded by the impeller's monitoring. The first three excitation frequencies

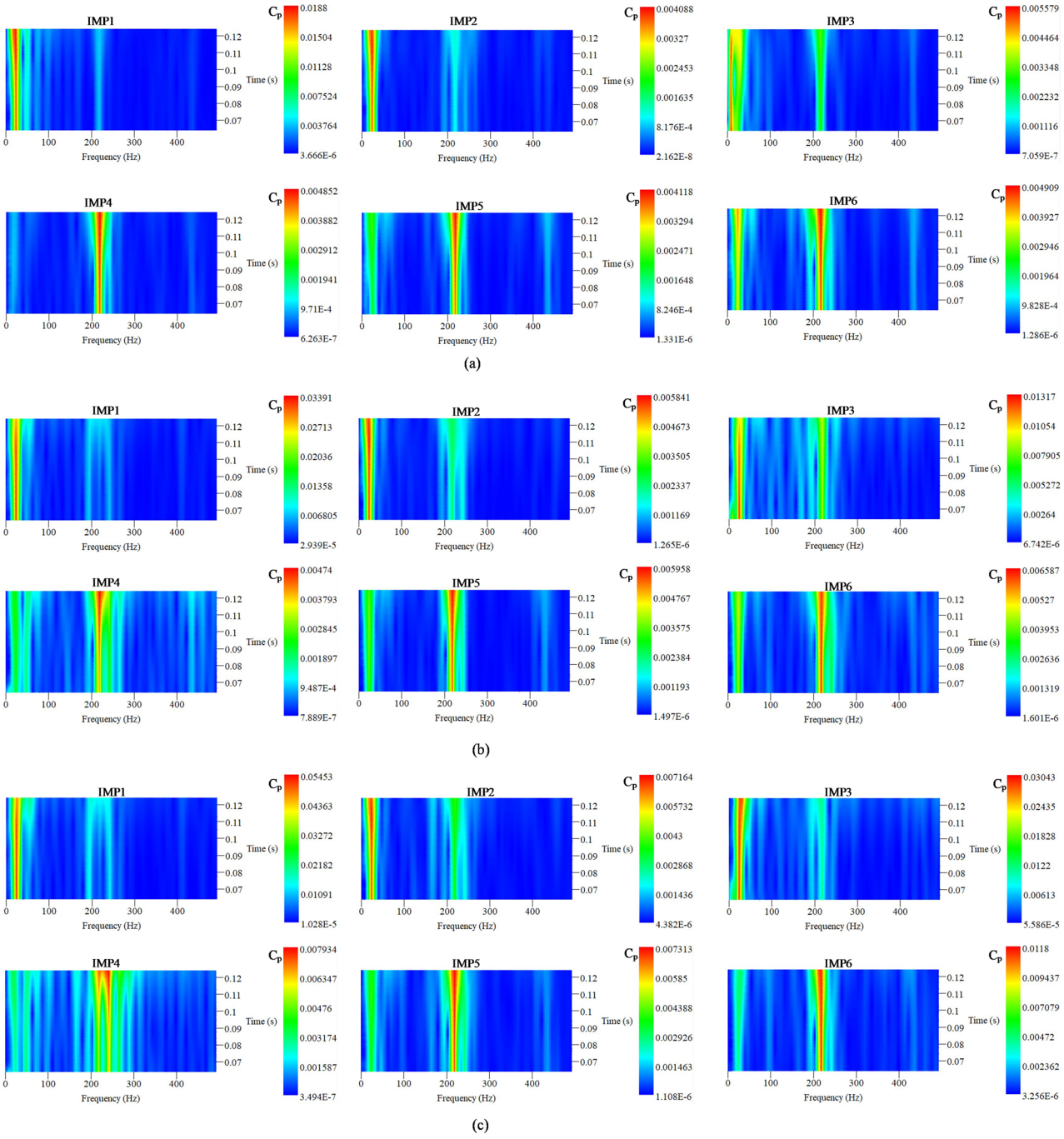

FIG. 18. Time–frequency domain of C_p within the impeller. (a) $0.8Q_d$, (b) $1.0Q_d$, and (c) $1.3Q_d$.

in the impeller occurred at 217.50 Hz ($9 \times f_n$), 435.00 Hz ($18 \times f_n$), and 652.50 Hz ($27 \times f_n$).

As shown in Fig. 21, the strength of the exciting pressure pulsation diminishes with increasing harmonic order k and m. Because the inherent frequencies of the structures are of the same order of magnitude as the exciting frequencies f_s and f_r, careful consideration of rotor–stator interaction is required for the design of mechanically safe turbines.

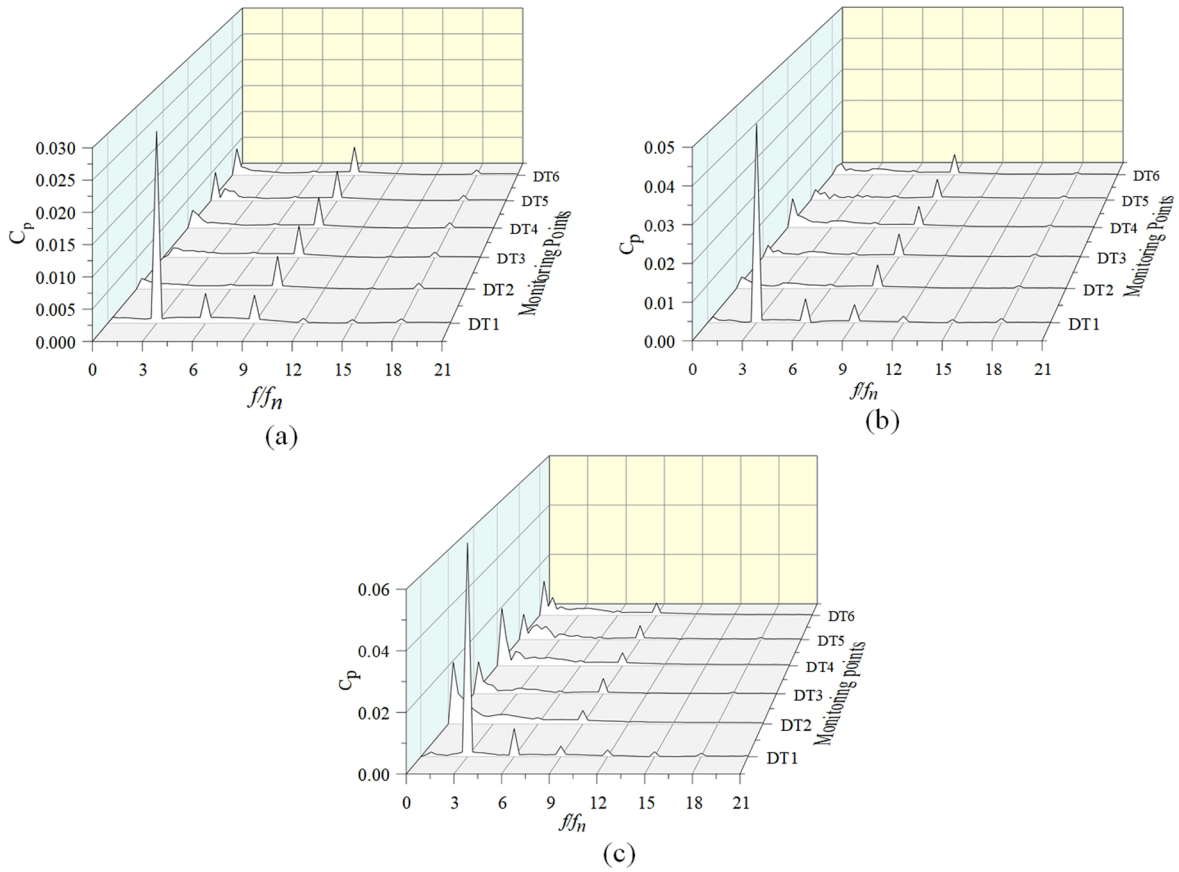

FIG. 19. Frequency-domain of C_p at within the outlet pipe. (a) $0.8Q_d$, (b) $1.0Q_d$, and (c) $1.3Q_d$.

E. Effect of change in the number of guide vane on harmonics

The number of guide vanes could influence the pulsation behavior of the parameters. The original choice of nine (9) blades was governed by manufacturing constraints rather than optimality for flow lines or vibration effect. Miroslav[30] proposed the number to determine based on hydraulic criteria of holding all the streamlines together, while Guthrie and Brown[31] and Raabe[32] not only consider hydraulic behavior but also mechanical behavior. They have recommended odd–even combination of runner and guide vanes numbers. In the investigated model (base model), the blades of the guide vane are chosen as nine, while the runner has three blades, which is an odd–odd combination. It would be interesting to see the effect of even–odd combination. Here, we change the guide vanes to eight (8) in number, while retaining the three on the runner. This is referred to as modified model [model with eight (8) vanes]. The 3D model and meshes of the modifications described above are presented in Fig. 22. The grids were drawn in accordance to the steps outlined in Sec. III A 1. All other geometrical parameters remained unchanged as well as the numerical setup.

Figure 23 depicts a comparative analysis of the frequency domain history of the pressure pulsations at the INL1-INL4, GV1-GV4, IMP1-IMP4, and DT1-DT4 as presented in Fig. 5.

From Fig. 23(a), a comparative frequency domain history of pressure pulsation of the base model with model with eight (8) guide vanes shows no significant effect on the harmonics. However, at $k = 1$ (BPF), the base model recorded peak amplitudes across all monitored points (INL1 to INL 4) in the inlet pipe. There is a transition in this trend at higher harmonics (from $k = 2$) where model with eight (8) vanes recorded peak amplitudes. A similar trend was observed at the guide vane and outlet pipe flow passage (represented by GV1 to GV4 and DT1 to DT4) as presented in Figs. 23(b) and 23(d), respectively.

Figure 23(c) depicts a comparative frequency domain plot of C_p at the impeller flow passage (IMP1 to IMP4) at $1.0Q_d$. There is a significant shift in the BPF due to a change in the vanes from nine (9) to eight (8). The first excitation frequency for the base model occurred at $f/f_n = 9$, but when the guiding vanes was changed to eight (8), the first excitation frequency occurred at $f/f_n = 8$, which is a true reflection of the guide vane number.

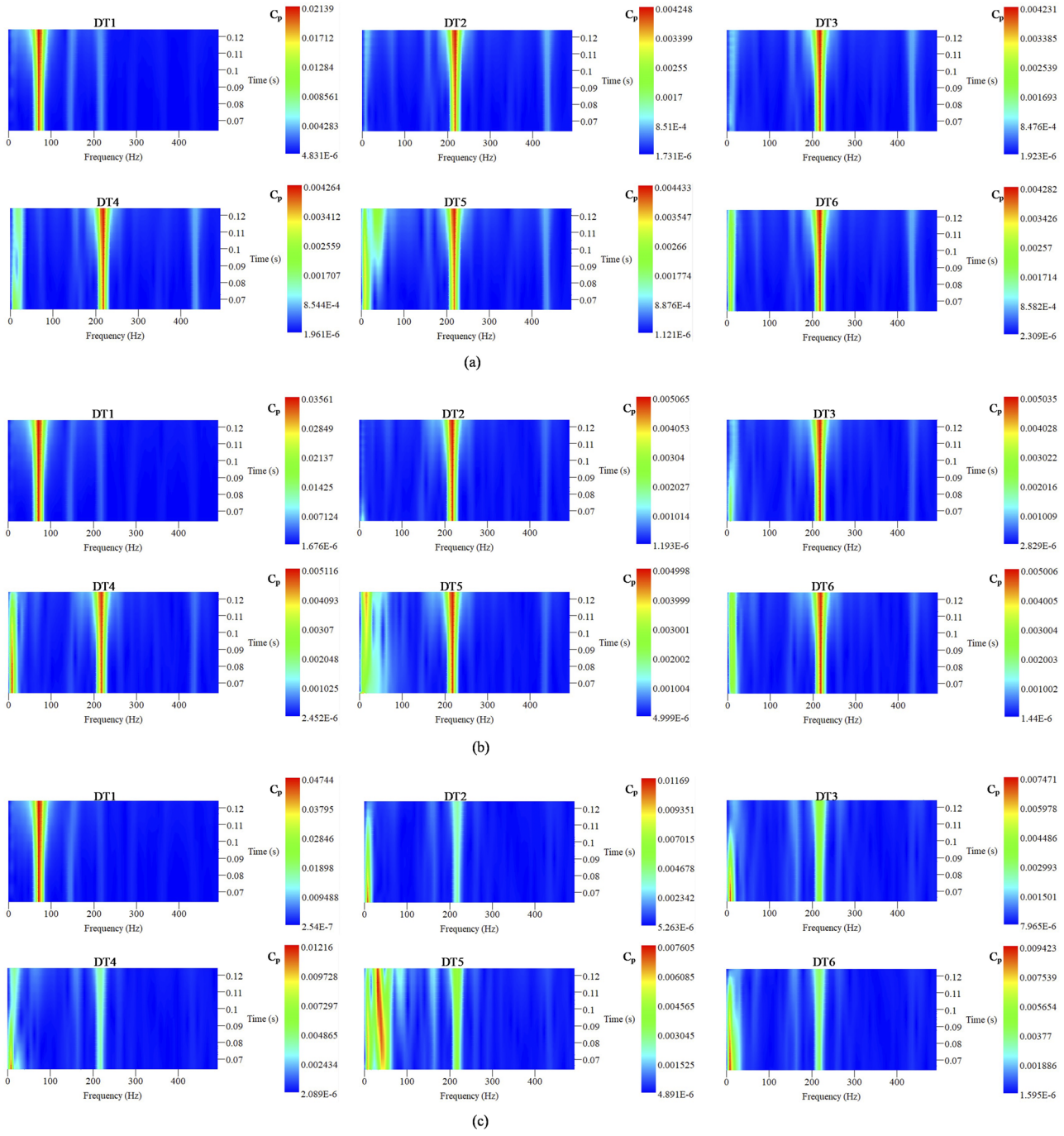

FIG. 20. Time–frequency domain of Cp within the outlet pipe. (a) $0.8Q_d$, (b) $1.0Q_d$, and (c) $1.3Q_d$.

F. Effect of straight inlet on harmonics

In the investigated model, the inlet pipe is at right angled shortly before the fluid flows into the guide vane. In view of the above scenario, straight inlet pipe was considered, and the resulting model is termed "model with straight inlet." The 3D model and meshes of the modification to the inlet pipe are presented in Fig. 24. The grids were drawn in accordance to the steps outlined in Sec. III A 1. All other geometrical

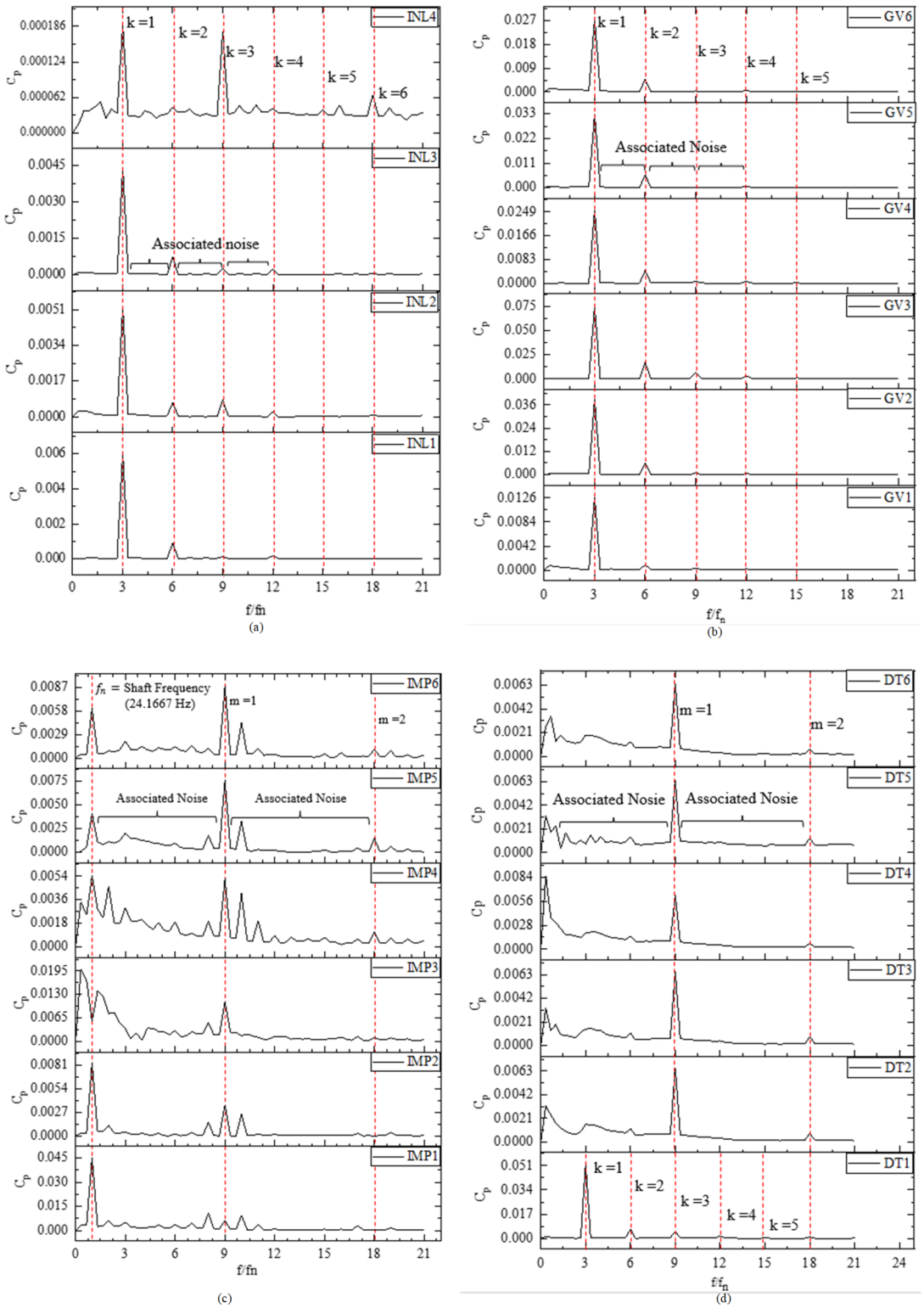

FIG. 21. Frequency analysis based on rotor–stator interaction at 1.0Qd. (a) Inlet pipe flow domain. (b) Guide vane flow domain. (c) Impeller flow domain. (d) Outlet pipe flow domain.

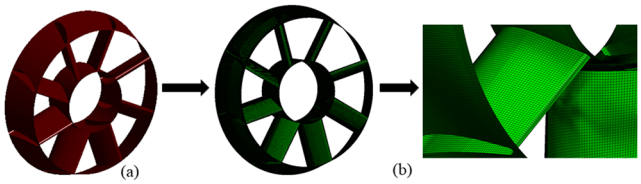

FIG. 22. Modified guide vane with eight (8) vanes. (a) 3D model. (b) Computational grid.

parameters remained unchanged as well as the numerical computational setup.

Figure 25 shows a comparative analysis of the frequency domain history of the pressure pulsations at the INL1-INL4, GV1-GV4, IMP1-IMP4, and DT1-DT4 as presented in Fig. 5.

From Fig. 25(a), a comparative frequency domain history of pressure pulsation of the base model with model with straight inlet shows no significant effect on the harmonics. However, at $k = 1$ (BPF), the base model recorded peak amplitudes across all

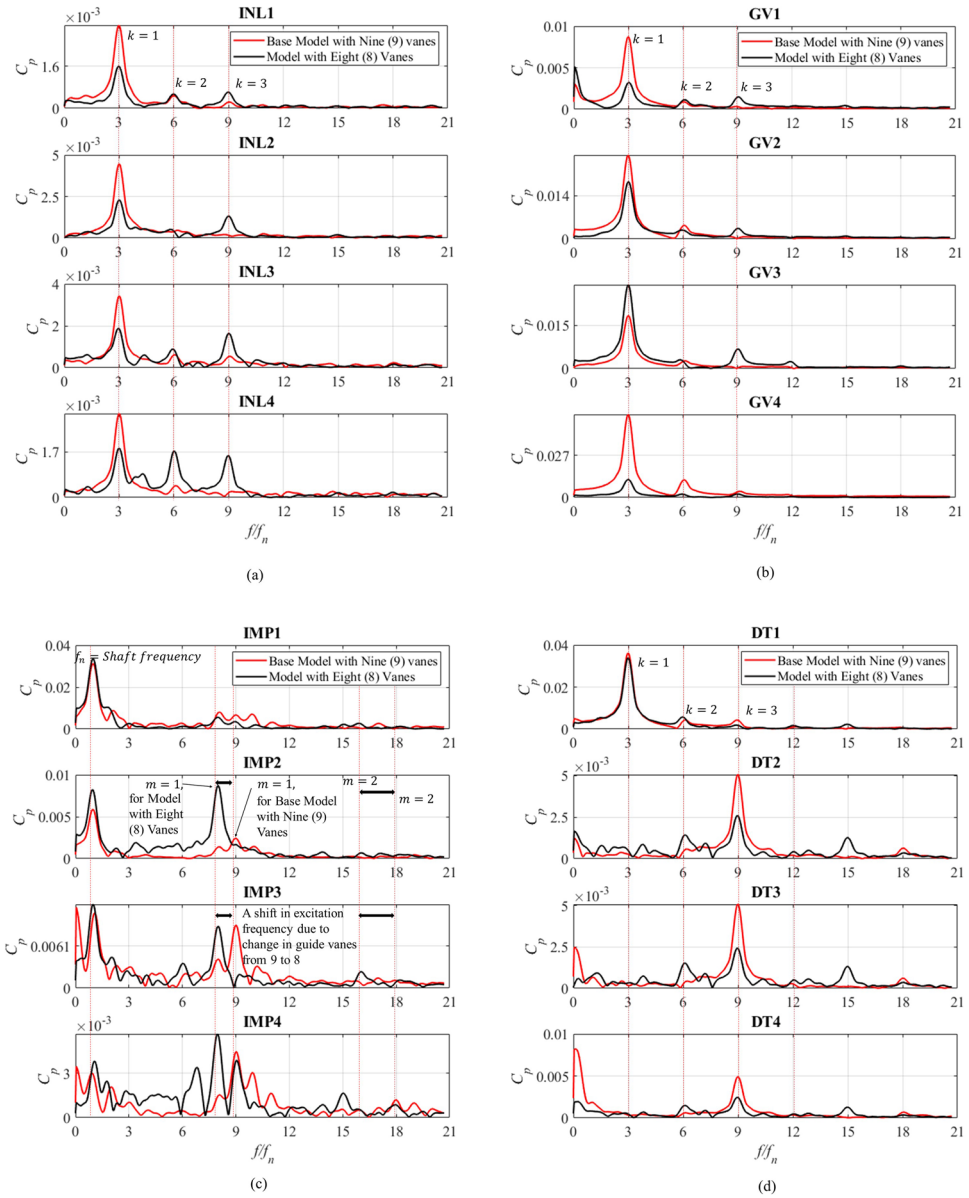

FIG. 23. Comparative frequency domain history at $1.0Q_d$. (a) Inlet pipe, (b) guide vane, (c) impeller, and (d) outlet pipe.

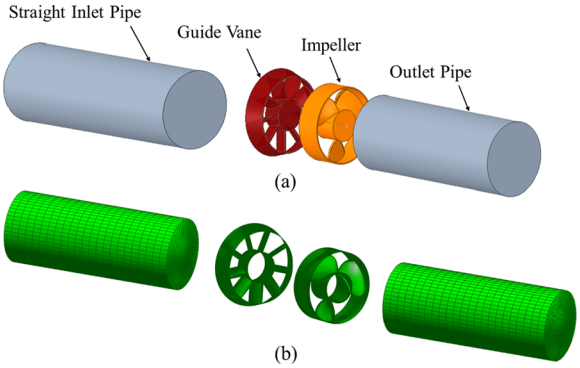

FIG. 24. Modified inlet pipe. (a) 3D model. (b) Computational grid.

monitored points (INL1 to INL 4) in the inlet pipe. A similar trend was observed at the guide vane, impeller, and outlet pipe flow passage (represented by GV1 to GV4, IMP1 to IMP4, and DT1 to DT) as presented in Figs. 25(b)–25(d), respectively.

Relatively, the amplitude of the pressure pulsation reduces when the inlet pipe is changed from right angled triangle to straight pipe inlet, but this change has little effect on the harmonics of the AFT.

Generally, the harmonics or excitation frequencies recorded at the stationary parts of the two new cases (model with straight inlet and model with eight vanes) are consistent with the result obtained from the base model in Sec. IV D. This is a strong indication that changing both the inlet pipe and the guide vane number has no effect on the blade passing frequency at the stationary flow domain.

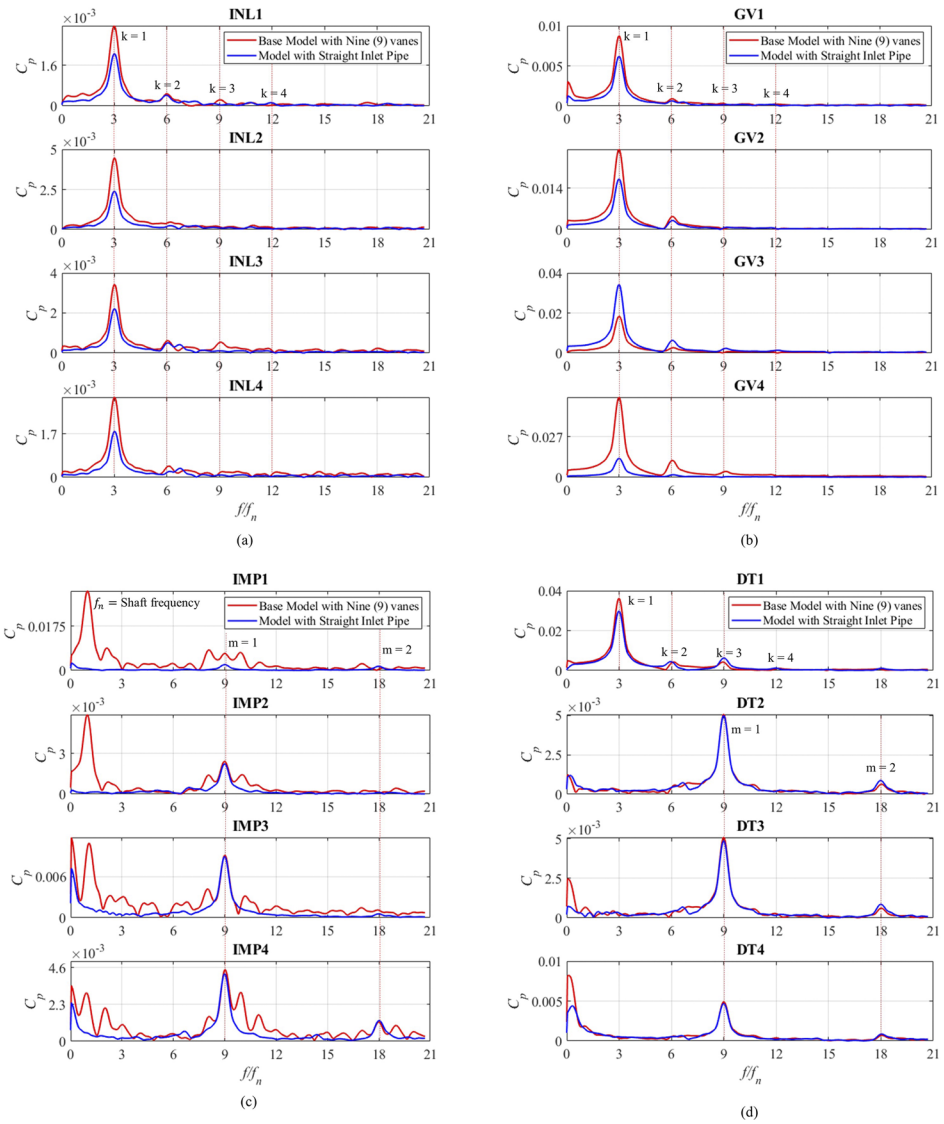

FIG. 25. Comparative frequency domain history at $1.0Q_d$. (a) Inlet pipe, (b) guide vane, (c) impeller, and (d) outlet pipe.

For the rotating flow domain, BPF for the model with straight inlet remained the same with the base model. However, a notable change in the BPF was recorded at the impeller due to changes in the number of guide vanes from nine (9) to eight (8). A shift from 217.50 Hz($9 \times f_n$) to 193.33 Hz($8 \times f_n$) was recorded. The results obtained in this section shows the strong effect of the RSI on periodic pressure pulsations and are consistent with Eqs. (22) and (23).

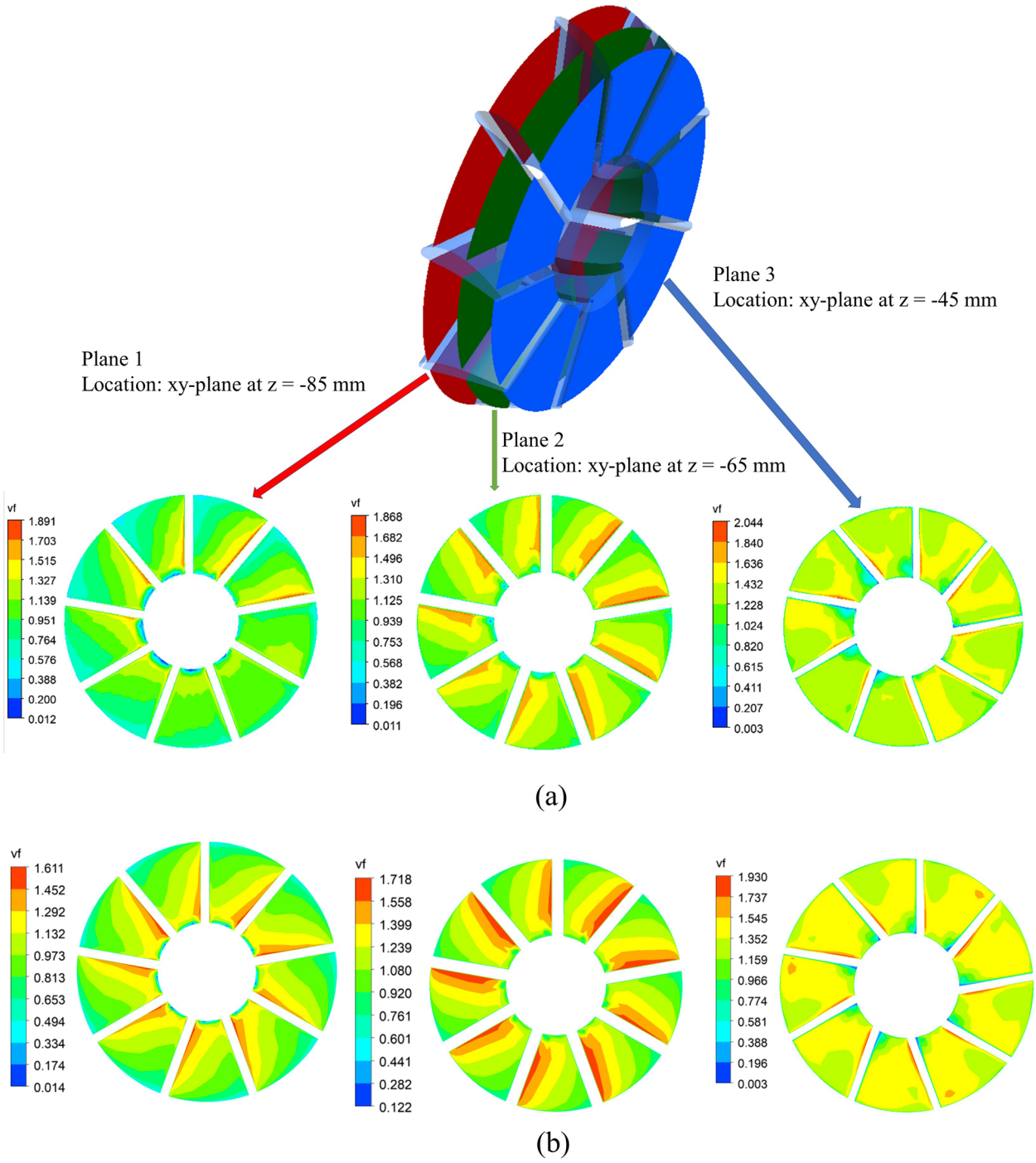

FIG. 26. Velocity fluctuation distribution v_f within the guide vane at $1.0Q_d$. (a) Base model. (b) Model with straight inlet.

G. Velocity fluctuation intensity in the guide vane with straight inlet

The velocity distribution in the guide vanes of the base model and model with straight inlet was analyzed and compared using velocity coefficient (vf) defined as the ratio of velocity (Vt) per timestep to the velocity at the tip of the impeller (see the following equation):

$$v_f = \frac{V_t}{U_2}. \tag{24}$$

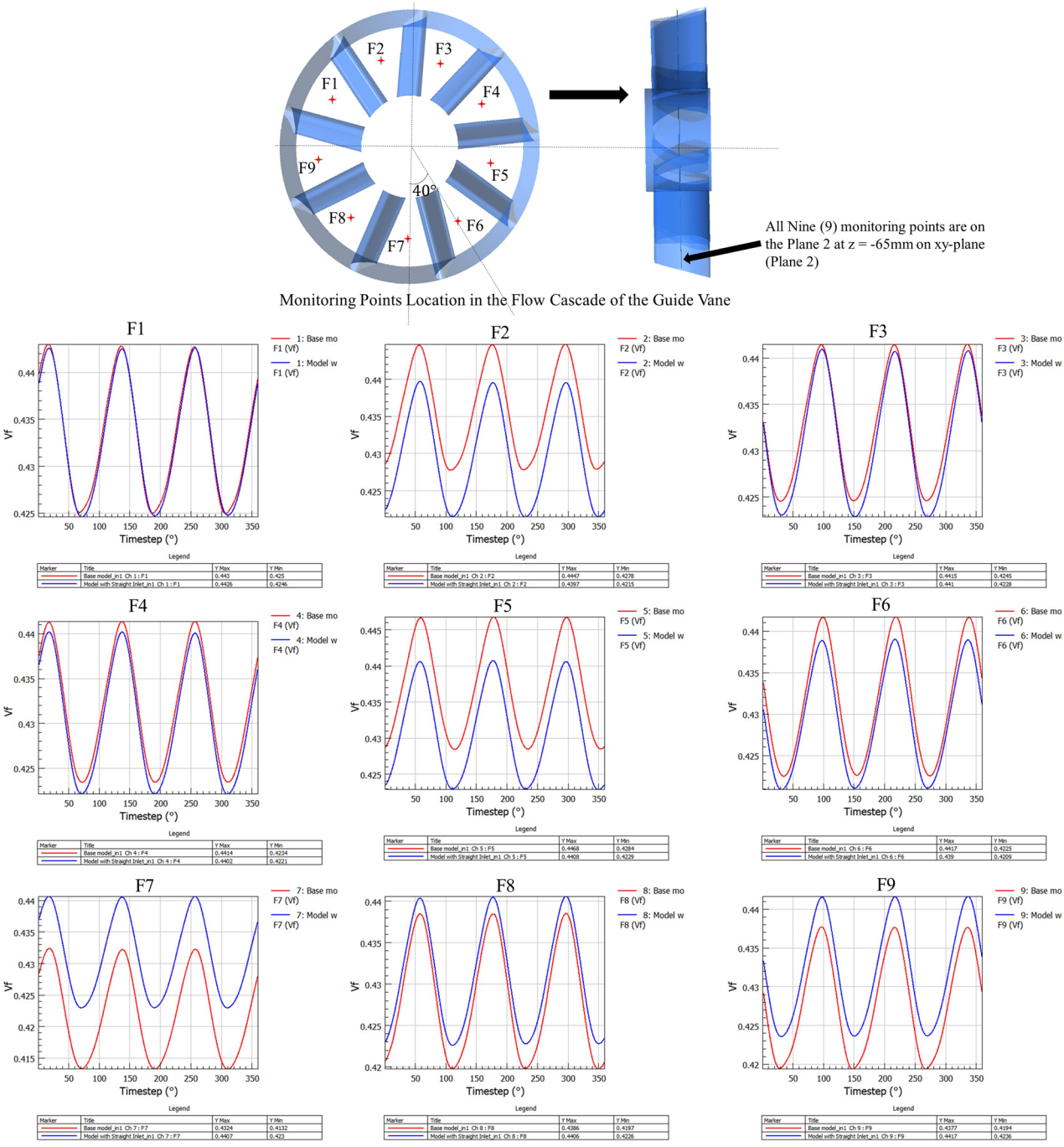

FIG. 27. Relative velocity fluctuation on the flow cascade of the guide vane.

Figure 26 depicts the intensity of the relative velocity fluctuation in the flow cascade of the guide vane at plane 1, plane 2, and plane 3, for the base model and model with straight inlet at $1.0Q_d$. There is an increasing trend in the velocity intensity from plane 1 to plane 2 up to plane 3. The above situation is attributed to the geometrical configuration of the guide vane aimed at increasing the fluid velocity and, at the same time, directing the fluid at a designated angle (angle of attack) to the impeller.

To further characterize the flow distribution in the guide vane of the AFT, monitoring points (F1, F2, F3, F4, F5, F6, F7, F8, and F9) were placed at plane 2, within the flow cascade of the guide vane to record the flow velocity per timestep to further delineate and quantitatively investigate the relative velocity for one complete revolution (see Fig. 27).

The velocity of the base model was found to be higher than model with straight inlet at F1 to F6, but a twist in this trend occurs from F7 to F9 where the relative velocity distribution of the model with straight inlet is higher than the base model.

V. CONCLUSION

The numerical and experimental pressure fluctuation intensity in a low head axial flow turbine has been successfully analyzed. The results shown by fluctuation intensities were recorded by the monitoring points within the flow channels of the turbine:

1. Unsteady numerical computation of the pressure fluctuation intensities in the turbine's inlet, guide vane, and outlet pipe depicts a qualitative agreement with experimental data.
2. The pressure fluctuation coefficients recorded on the time domain history plots reveal a steady decrease from inlet to outlet except at the impeller, where an increase was observed around the leading edge through the pressure side before decreasing at the trailing edge. Three regular pressure pulses were recorded in one complete revolution at all monitoring points in the static components (inlet pipe, guide vane, and outlet pipe). A different trend was observed in the impeller where nine regular pressure pulses were observed.
3. The excitation frequencies in the stationary parts occurred at 72.5 Hz $(3 \times f_n)$, 145.00 Hz $(6 \times f_n)$, and 217.5 Hz $(9 \times f_n)$. In addition, the excitation frequency in the impeller occurred at 217.5 Hz $(9 \times f_n)$, 435 Hz $(18 \times f_n)$, and 652.5 Hz $(27 \times f_n)$.
4. The time and frequency data reveal the influence of the rotor (impeller)–stator (guide vane) interaction as the flow changes through the turbine. The flow exchange between the guide vane and impeller is culpable for the pressure pulses, which subsequently influences vibration and noise generated in the turbine.
5. The impeller recorded maximum pressure pulsations since the monitoring point sweeps through the nine (9) guide vanes, generating nine peaks and valleys in one revolution. However, a change in the guide vane to eight generated eight peaks and valleys. The excitation frequency resulting from the changes in the vanes from nine to eight in the impeller occurred at 193.34 Hz $(8 \times f_n)$, 386.67 Hz $(16 \times f_n)$, and 580.01 Hz $(24 \times f_n)$.
6. The frequency-domain history for the 90° bend inlet reveals an increase in the amplitude of pressure pulsation intensity with rising flow rate from part load $(0.8\ Q_d)$ through design flow $(1.0\ Q_d)$ to overload $(1.3\ Q_d)$. However, when the straight inlet pipe was used, the amplitude of the pressure pulsation reduces across all monitoring points compared with the values of C_p recorded by 90° bend entry. The changes in the inlet pipe has no significant effect on the harmonics recorded in the turbine, but its effect on the distribution of v_f is significant since it influences the velocity distribution in the guide vane flow passage. Majorly, the model with 90° bend entry recorded higher v_f in the flow passage of the guide vane while the model with straight entry accounted for the least v_f.

Conclusively, the authors hope that the reported results will enlighten and serve as reference resource on unsteady pressure fluctuation leading to the optimization and stable operation of axial flow turbine.

ACKNOWLEDGMENTS

This study was financially supported by the Youth Fund Project of Jiangsu Natural Science Foundation (Grant No. BK20180876), the Major Cultivation Project of Sichuan Provincial Department of Education (Grant No. 18cz0016), and the Key Project of Xihua University (Grant No. z2010810). The supporters are gratefully acknowledged. The authors would also like to thank the anonymous reviewer who recommended the study of pulsation characteristics due to guide vane number and mode of flow entry into the axial flow turbine.

AUTHOR DECLARATIONS

Conflict of Interest

The authors have no conflicts to disclose.

NOMENCLATURE

C_p	coefficient of pressure fluctuation intensity
D	diameter of the impeller
e	dissipation of kinetic energy of turbulence
f_n	shaft frequency
$F1$	blending or auxiliary functions in the turbulence model
g	acceleration due to gravity
H	head
k	kinetic energy of turbulence
M	torque
N	rotational speed
n_s	specific speed
P	pressure
Q	flow rate
t	time
U_2	circumferential velocity of the impeller outlet
u_i	velocity components (u, v, w) in Cartesian directions$x$, y, z
x, y, z	coordinates in stationary frame
z	blade number
β^*, γ	turbulence-model coefficients
Γ	auxiliary variables in the turbulence model
Δ	difference

δ_{ij}	Kronecker's delta
η	efficiency
μ	dynamic viscosity
μ_T	turbulent viscosity
ρ	density
σ_k, σ_ω	turbulence-model coefficients

Subscripts

0	origin
gv	guide vane
i, j	components in different directions
x_i	Cartesian coordinates: x, y, z

Abbreviations

3D	three dimensional
AFT	axial flow turbine
BPF	blade passing frequency
CFD	computational fluid dynamics
DT	outlet pipe flow passage
FFT	fast Fourier transformation
GV	guide vane flow passage
IMP	impeller flow domain
INL	inlet pipe flow domain
RANS	Reynolds-averaged Navier–Stokes
SST	shear stress transport

DATA AVAILABILITY

The data that support the findings of this study are available within the article.

REFERENCES

[1] R. G. Iovănel, D. M. Bucur, G. Dunca, and M. J. Cervantes, IOP Conf. Ser.: Earth Environ. Sci. **240**, 022046 (2019).

[2] D. Ni, N. Zhang, B. Gao, Z. Li, and M. Yang, Energy **198**, 117305 (2020).

[3] K. Amiri, M. J. Cervantes, and B. Mulu, J. Hydraul. Res. **53**, 452 (2015).

[4] S. F. Harding and M. C. Richmond, Report No. PNNL-26061, 2017, p. 48.

[5] S. Houde, R. Fraser, G. Ciocan, and C. Deschênes, IOP Conf. Ser. Earth Environ. Sci. **15**, 062061 (2012).

[6] T. Chirag, M. J. Cervantes, G. Bhupendrakumar, and O. G. Dahlhaug, J. Hydraul. Res. **52**, 283 (2014).

[7] A. Rivetti, C. Lucino, and S. Liscia, Am. J. Hydropower, Water Environ. Sytems **1**, 34 (2014).

[8] E. M. Greitzer, C. S. Tan, and M. B. Graf, *Internal Flow* (Cambridge University Press, 2004).

[9] P. Dörfler, M. Sick, and A. Coutu, *Flow-Induced Pulsation and Vibration in Hydroelectric Machinery* (Springer, London, 2013).

[10] ISO_354, 61010-1 © IEC2001 2003, p. 13, 2003.

[11] A. Javadi and H. Nilsson, Int. J. Heat Fluid Flow **63**, 1 (2017).

[12] H.-H. Kim, M. Rakibuzzaman, K. Kim, and S.-H. Suh, Energies **12**, 264 (2019).

[13] X. Sang, X. Zhou, X. Liu, and X. Hao, J. Vibroeng. **19**, 1332 (2017).

[14] M. Zhang, D. Valentín, C. Valero, M. Egusquiza, and E. Egusquiza, Eng. Failure Anal. **97**, 690 (2019).

[15] M. Zhang, D. Valentin, C. Valero, A. Presas, M. Egusquiza, and E. Egusquiza, Eng. Failure Anal. **109**, 104389 (2020).

[16] X. Song and C. Liu, Adv. Mech. Eng. **11**, 1 (2019).

[17] X. Song and C. Liu, Renewable Energy **145**, 2327 (2020).

[18] L. Shi, Y. Yuan, H. Jiao, F. Tang, L. Cheng, F. Yang, Y. Jin, and J. Zhu, Renewable Energy **163**, 987 (2021).

[19] P. Gudmundson, Proc. ASME Turbo Expo **5**, 249 (1982).

[20] E. H. Dowell, K. C. Hall, and M. C. Romanowski, Appl. Mech. Rev. **50**, 371 (1997).

[21] P. Moinier and M. B. Giles, J. Propul. Power **21**, 973 (2005).

[22] K. C. Hall and C. B. Lorence, in *ASME 1992 International Gas Turbine and Aeroengine Congress and Exposition (GT1992)* (Journal of Turbomachinery, 1992), Vol. 5.

[23] I. B. Celik *et al.*, J. Fluids Eng. **130**, 078001 (2008).

[24] F. Menter, in *23rd Fluid Dynamics, Plasmadynamics, and Lasers Conference* (American Institute of Aeronautics and Astronautics, Reston, Virigina, 1993).

[25] D. C. Wilcox, AIAA J. **32**, 247 (1994).

[26] I. Božić and M. Benišek, Renewable Energy **94**, 537 (2016).

[27] M. H. Sotoude Haghighi, S. M. Mirghavami, S. F. Chini, and A. Riasi, Renewable Energy **135**, 266 (2019).

[28] M. Hadi, S. Haghighi, S. M. Mirghavami, M. M. Ghorani, A. Riasi, and S. F. Chini, Renewable Energy **147**, 409 (2020).

[29] ANSYS CFX-Solver Theory Guide, 2020.

[30] N. Miroslav, *Hydraulic Turbines Their Design and Equipment* (Artia, 1957).

[31] J. Guthrie Brown, *Hydro-Electric Engineering Practice*, 2nd ed. (Blackie, Glasgow; London, 1964).

[32] J. Raabe, *Hydro Power: The Design, Use and Function of Hydromechanical Hydraulic, and Electrical Equipment* (VDI-Verlag, 1985).